SYNTHESIS, CHARACTERIZATION, AND BIOLOGICAL ACITVITY OF ALUMINUM SUBSTITUTED HYDROXYAPATITE AND AMORPHOUS CALCIUM PHOSPHATE

A Thesis

Presented to the Faculty of the Graduate School

of Cornell University

In Partial Fulfillment of the Requirements for the Degree of

Master of Science

by

Joo Ho Kim

August 2017

ABSTRACT

Hydroxyapatite (HA; $Ca_{10}(PO_4)_6(OH)_2$) is an inorganic crystalline material found in biological hard tissues, such as bone and teeth. Biogenic HA is non-stoichiometric and has varying crystallinity and ionic substitutions depending on the function and anatomy of the tissue within which HA occurs. HA is also found in pathological calcifications, such as microcalcifications (MCs) found in breast cancer tissues. HA MCs with lower carbonate substitution have shown to be related to more invasive (malignant) breast cancer tissue specimens, suggesting pathological connections to ionic substitutions in HA. Recently, aluminum substitution in HA MCs was identified but its connection to cancer progression remains unclear. To further understand aluminum substitution in HA and its relevance to cancer, aqueous synthesis and thorough characterization of aluminum substituted HA (Al-HA) was done via powder X-ray diffraction, Fourier-transform spectroscopy, X-ray photoelectron spectroscopy and electron microscopy (SEM, TEM). With increasing concentrations of aluminum in particle synthesis morphologies of particle became elongated and thinner compared to a rod-like shaped HA particle morphology. Also with high concentrations of aluminum inclusion, particles no longer maintained long-range crystalline order, and aluminum substituted amorphous calcium phosphate (Al-ACP) was formed. Utilizing the synthesized HA, Al-HA, and Al-ACP particles, three-dimensional porous poly(lactic-co-glycolic acid) cell culture scaffolds were fabricated to mimic the microenvironment of aluminum substituted MCs found in breast tissues. Breast cancer cells (MDA-MB231) were seeded and cultured *in vitro* to assess the

effect of Al-HA and Al-ACP on cell adhesion. Compared to blank scaffolds, cells adhered better on HA and Al-HA containing scaffolds. Whereas, compared to HA containing scaffolds, cells adhered less on Al-ACP containing scaffolds. This research lays the groundwork for future studies to investigate the role of Al-HA in breast cancer diagnosis and prognosis.

BIOGRAPHICAL SKETCH

Joo Ho Kim was born on 1989 in Seoul, South Korea. He loved reading about dinosaurs and space as a toddler, which eventually led him to appreciate and enjoy studying science in school. He then went to Hanyang University in Seoul to study in Materials Science and Engineering. Studying metallurgy and ceramics science and engineering guided him to culminate motivation to deeper understand the laws of nature and to gain interest in expanding his knowledge into biological applications of materials.

Joo Ho joined Dr. Dongyoung Kim's laboratory in Korea Institute of Science and Technology (KIST) to conduct research on developing functionalized carbon nano-tubes for glucose biosensor applications. From KIST he learned to perform in research environments and to respect the working of science and engineering.

Joo Ho joined Prof. Lara Estroff's research group in the Department of Materials Science and Engineering at Cornell University in September 2015. He focused on synthesizing and characterizing aluminum substituted hydroxyapatite, which he later further went to apply the materials for breast cancer studies. After graduation, he will continue his studies at Johns Hopkins University for a doctorate degree and pursue his interest in biomaterials.

DEDICATIONS

To the ones I trust and had faith in me

ACKNOWLEDGMENTS

I thank everybody that I have met and learned from during the past 2 years in Cornell. I especially thank Professor Lara Estroff, my advisor. She has given me the best support I could ever get as a Masters student. Her enthusiasm towards science was truly contagious and kept me motivated to pursue research. And thanks to her patience, I was able to focus and enjoy all aspects of research processes. I also thank my minor chair member, Professor Eve Donnelly. Without her support, I would have not been able to finish my program. I thank Professor Claudia Fischbach-Teschl and her group member for helping me get accustomed to biology laboratories. I thank Frank He and Jennie Kunitake for teaching me, I have learned not only science but also things beyond science and research from them. Estroff group members were the best people to have around. I thank them for showing me how we can nourish each other to become better. I thank my family for all their support and love.

TABLE OF CONTENTS

LIST OF FIGURES

LIST OF TABLES

Chapter 1.

Introduction and Background

1.1 Ionic substitutions in hydroxyapatite

Numerous biological species contain hydroxyapatite (HA) in their inorganic part of hard tissues (e.g., bone and teeth) and in these tissues, HA is never in pure stoichiometric form ($Ca_{10}(PO_4)_6(OH)_2$). Rather, multiple ionic substitution to HA are observed in nature and pure HA mineral is rare to find outside the laboratory. Based upon these observations, there is much research on the biological effects of various ion substituted HAs.

Depending on the organism and/or the anatomic location of the hard tissues, the degree of substitution of individual trace elements in HA varies. Other than calcium and phosphorous (or phosphate), all organisms have a variety of trace elements substituted in HA (Table 1.1). All of these elements are in different ratios

Table 1.1. Inorganic elemental content of bone in different organisms and different parts of human hard tissues (in wt%; '-'indicates undetected or in extremely minute quantity neglected by the authors)[1,18,42]

Sample Species	Ca	P	Na	Mg	K	Fe	Zn	Mn	Sr	Cl	F
Teleostomi (Bony Fish)											
Sea bream	35.4	17.5	0.81	0.54	0.215	47ppm	109ppm	41ppm	-	-	-
Norse Mackerel	35.8	17.3	0.38	0.52	0.657	117ppm	85ppm	16ppm	-	-	-
Carp	35.6	16.9	1.01	0.61	0.199	39ppm	280ppm	21ppm	-	-	-
Tuna	41.84	17.34	0.63	0.31	0.03	-	-	-	0.07	-	-
Swordfish	41.80	17.37	0.57	0.32	0.05	-	-	-	0.07	-	-
Elasmobranchii (Cartilegenous Fish)											
Shark	34.9	16.9	1.55	0.42	0.373	27ppm	91ppm	48ppm	-	-	-
Eutheria (Mammal)											
Cattle	36.5	17.2	0.85	0.81	0.340	267ppm	209ppm	1.4ppm	-	-	-
Swine	36.9	17.0	0.77	0.66	0.364	114ppm	218ppm	1.1ppm	-	-	-
Neornithes (Modern Bird)											
Fowl	36.1	17.4	0.84	0.70	0.490	376ppm	340ppm	4.8ppm	-	-	-
Human											
Enamel	37.6	18.3	0.70	0.2	0.05	118ppm	263ppm	0.6	0.03	0.4	0.01
Dentine	40.3	18.6	0.1	1.1	0.07	93ppm	173ppm	0.6	0.04	0.27	0.07
Bone	36.6	17.1	1.0	0.6	0.07	-	39ppm	0.17	0.05	0.1	0.1

depending on the organism and it can be assumed that these differences in ratios are related to the environmental (i.e., habitats) and biological differences between organisms. For example, different constituents between freshwater and saltwater fish bones suggests that habitat conditions influence the composition of elements [1]. This trend is further exemplified by the different composition of hard tissues between terrestrial and marine life. In the end of Table 1.1, the elemental content of bone in different parts of human body are different, which points to the fact that different levels of ionic substitution in HA leads to different functionalities.

Biogenic HA, along with ionic substitution, is found in varying crystallinity, solubility, stability, ionic substitution, coordination and more depending on the function and anatomy of the tissue within which the HA occurs [2–4]. In this thesis, the term "physicochemical property" will be referring to mainly crystallinities and ionic substitutions in HA. Crystallinity of HA particles in bone differ from different anatomy and it can be used to measure bone quality [5–7]. Bone mineral maturity (ratio of apatitic domain and non-apatitic domain) is related to HA crystallinity, where mineral maturity is closely related to overall bone remodeling mechanism mediated by osteoblasts and osteoclasts [8–12]. Protein adsorption to HA particles are strongly effected by crystallinity of HA which is further relevant to cell responses [13–16]. Ionic substitution in HA can also play a role in functionalizing hard tissue [4,10,17–20]. Magnesium ions were found to be localized on the grain boundaries of rodent enamel, implying functionality of wear and tear resistance of magnesium substitution to HA [4]. Strontium substituted HA has been synthesized and have shown potential in bone regenerative medicine [20]. As mentioned above, studies show that physicochemical

properties of HA in bone affects and modulates the hard tissue functionalities. These reports further guides us to understand the importance of nanoscale characteristics of materials in bone.

HA is also found in microcalcifications (MCs) of pre-cancerous and cancerous breast-tissues and it is often detected and used for prognosis of cancer's malignancy in mammograms. In terms of MC's material phase, HA is found to be associated with more malignant cases of breast cancer compared to calcium oxalate found in MCs of healthy or benign cases of breast lesions. Nanoscale properties of bone have shown to play a role in biology, and there are increasing reports of such nanoscale physicochemical properties of MC's material related to progression of pathology [21–23, 43]. Degree of carbonate incorporation in MCs has been shown to be relevant to the breast cancer progression [24]. Ratio of material types found in MCs have also shown to be correlated to breast cancer's malignancy [23]. Also recently, aluminum incorporation in HA MCs was found in pre-cancerous breast tissues [43].

Biological research on interactions of elements in individual systems is important, and detailed observations of how elements get incorporated into hard tissue can explain different mechanisms of inorganic mineralization of hard tissues and its role in biology. In this extent, understanding the HA crystal structure and how different ions are being incorporated into the structure will provide fundamental explanations to how imperfect biogenic HAs interact with biology.

1.2 Hydroxyapatite structure

Hydroxyapatite is one of the most stable and insoluble phases of calcium orthophosphate minerals [18]. HA and ion substituted HA can be synthesized via various methods such as sol-gel, hydrothermal, mechanochemical, aqueous precipitation methods and others [25]. Despite the various syntheses available, this thesis will focus on ion substituted HA synthesized through aqueous precipitation method. Aqueous precipitation is an easy and safe route for synthesizing HA, yielding a bio-friendly product. Also, precipitation method is considered to be similar to the actual nucleation and growth occurring in the ion rich environment of organisms [18].

To discuss ion substituted HA, we must understand the crystallographic structure of HA. Lattice parameters of the hexagonal stoichiometric HA unit cell are: a = 0.9430 nm and c = 0.6891 nm [25]. Hexagonal HA contains 10 calcium, 6 phosphate, and 2 hydroxyl ions in its unit cell. This specific number of ions in a unit cell sums up to ionic charge neutrality. Researchers often utilize the Ca/P ratio to identify certain phases of calcium phosphate minerals. Stoichiometric (pure) HA has a Ca/P ratio of 1.67 and commonly found biogenic HA have Ca/P ratios ranging from 1.61 to 1.71 [26,27].

Understanding the structure of ions packed in HA is important when we want to determine how foreign ions are being incorporated to the HA crystal lattice. Different sites available in the structures exert different adjustments to the overall crystal structure, size, morphology, and potentially, its biological interactions.

Two Ca sites are distinguished as Ca(I) and Ca(II), derived from their different local environments within the unit cell. Ca(I) is also known as columnar Ca, and is

located on the 6 corners of the hexagonal unit cell. Whereas Ca(II) is known as channel Ca, reflecting its formation of a hexagonal channel in the middle of the unit cell. (Figure 1.1)

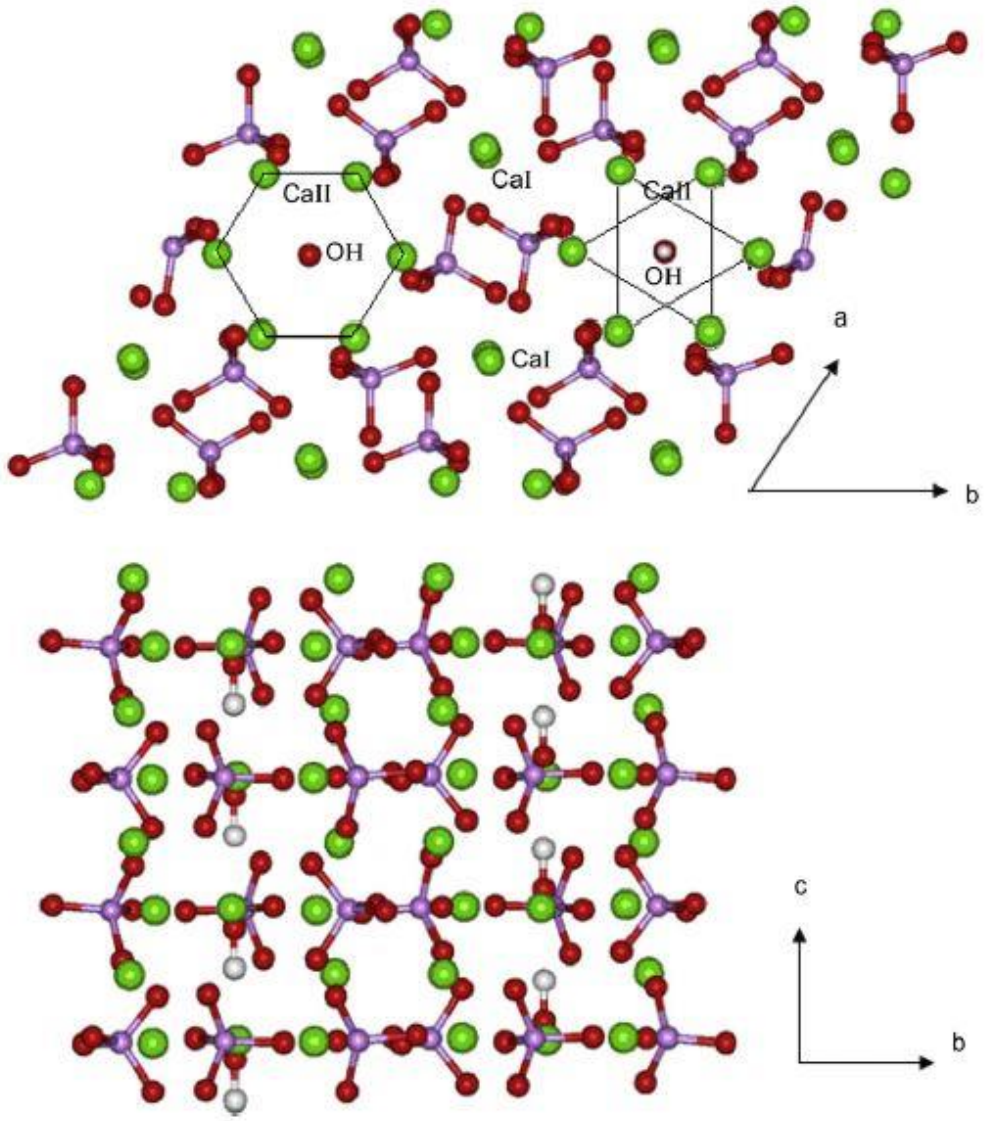

Figure 1.1. Representation of the HA structure perpendicular to the crystallographic c-axis and a-axis. Showing different types of Ca sites. (Ca =Green, O = Red, P = Purple, H = White) [41]

Each Ca(I) ion is bonded to 9 oxygens, 6 of which are tightly bonded (Figure 1.2). Multiple Ca-O bonding environments and strictly aligned Ca(I) ions in columns

maintains the overall unit cell structure, thus small changes in this Ca(I)-O bond will significantly alter the entire lattice.

Each Ca(II) ion is bonded to 7 oxygens, (Figure 1.2) and triangular layers of Ca(II) ions are stacked in an alternating manner (Figure 1.1). Because of this less rigid stacking of Ca(II), some alterations of Ca(II)-O bonds are tolerated and the unit cell structure is maintained. Two consecutive triangular layers of Ca(II) form a hexagonal channel in the center of the unit cell along the c-axis.

In the hexagonal channel formed by Ca(II) ions, two OH^- ions exist, where all the hydrogen part of the OH^- ions in a channel either points upward or downward. Such alignment of OH^- ions take part in inducing minute strain to the structure, which further promotes ionic substitution in its vicinity. It should also be noted that OH^- ions in the unit cell are slightly above the Ca(II) ions triangular plane, implying a room for structure stabilization via alteration of OH^- or Ca(II) ions.

Phosphate (PO_4^{3-}) tetrahedral groups can be visualized as Ca ion connecting building blocks within the unit cell. A single PO_4^{3-} ion is surrounded by five Ca(II) and four Ca(I) ions (Figure 1.2). Six different PO_4^{3-} ions are bonded to Ca(I) ion by either one or two oxygens from each PO_4^{3-} ions, which in total of nine oxygens are coordinated to Ca(I). Five different PO_4^{3-} ions are bonded to Ca(II), which are six of its seven oxygen coordination. The remaining oxygen coordination is from OH^- ion.

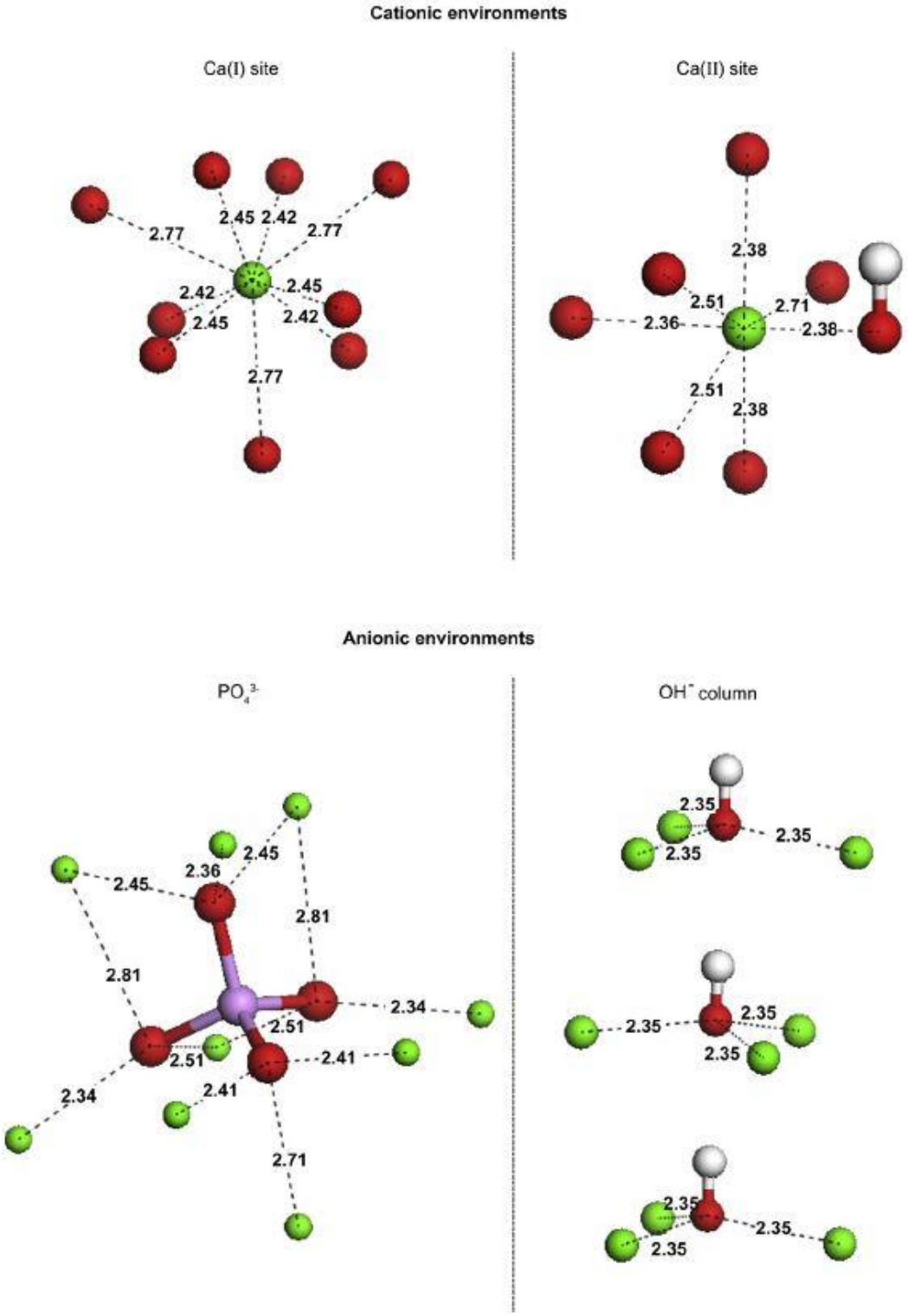

Figure 1.2. Representation of the local environment of the cations and anions in HA, with indication on the coordination distances (in Angs.) around each ion . Note that Ca(I)-O bond lengths are longer than Ca(II)-O bond length in average. (Ca= Green, O= Red, P= Purple, H= White) [41]

From the structure of pure HA, we can deduce the factors to help us understand ionic substitutions in HA. 1) The four available substitution site (Ca(I), Ca(II), PO_4^{3-}, OH^-). 2) Relevance of ionic radius of the substituent. 3) Adoptable coordination states of the substituents. 4) Charge of substituent ions.

1.3 Aluminum and aluminum substituted hydroxyapatite

Aluminum can be introduced to the human body from a number of sources. Oral consumption of aluminum can occur from food preservative, containers, and certain gastrointestinal protectants [28]. Aluminum is also included in vaccine adjuvants and antiperspirant products, which are the sources of trans-percutaneous or percutaneous introduction of aluminum to humans [29–32]. Reports have shown accumulation of aluminum in regions of tissue is associated with pathology. For example, usage of aluminum containing phosphate binders for treating patients with renal failure have shown to increase aluminum localization in brain and bone causing encephalopathy and osteomalacia [33]. Aluminum is also suggested to be pathologically associated with breast cancer [30–32,34,35]. Aluminum detection have been reported in nipple aspirate fluids (NAF) with higher quantities in breast cancer patients [30,31,36]. Additionally, aluminum was also found localized in HA MCs in pre-cancerous breast tissues [43], which in particular was of our interest of inquiry.

Studies of aluminum substituted HA (Al-HA) syntheses, such as aqueous precipitation method, ion-exchange method, and combustion method have been explored regarding the effect of aluminum on particle morphologies [37–39]. Fewer studies have been done to understand the biological effects of synthetic Al-HA. Wang

et al. conducted cytotoxicity assay on leachates of Al-HA in culture media and observed increasing fibroblast (L929) cytotoxicity with more concentrated leachate media [40]. Kolekar et al. conducted cytotoxicity assay of fibroblast (L929) cells incubated with combustion method synthesized Al-HA suspended in media and observed no significant differences of cytotoxicity with varying aluminum concentration in Al-HA [39]. Two studies mentioned above have approached cell experiments in the context of bone pathology (i.e. osteomalacia). Also, the cell experiments [39,40] were designed to indirectly assess the effect of Al-HA on cells.

Current studies done on Al-HA have been mainly focused on bone health and direct inquiry of Al-HA related to breast cancer is absent. Additionally, the field has been experiencing difficulty of finding a robust and biologically relevant *in vitro* cell culture system to assess the effect of stationary biomaterial particles. The aims of this thesis are to, 1) characterize biologically relevant Al-HA particles synthesized through aqueous co-precipitation, 2) apply Al-HA particles in three dimensional cell culture scaffold system mimicking *in vivo* microenvironments, and 3) lay the groundwork for understanding the role of Al-HA involved MCs in breast cancer progression.

1.4 References

1. Hamada, M., Nagai, T., Kai, N., Tanoue, Y., Mae, H., Hashimoto, M., Miyoshi, K., Kumagai, H. & Saeki, K. Inorganic Constituents of Bone of Fish. *Fish. Sci.* **61,** 517–520 (1995).

2. Asscher, Y., Weiner, S. & Boaretto, E. Variations in atomic disorder in biogenic carbonate hydroxyapatite using the infrared spectrum grinding curve method. *Adv. Funct. Mater.* **21,** 3308–3313 (2011).

3. Pasteris, J. D., Wopenka, B., Freeman, J. J., Rogers, K., Valsami-Jones, E., van der Houwen, J. A. M. & Silva, M. J. Lack of OH in nanocrystalline apatite as a function of degree of atomic order: Implications for bone and biomaterials. *Biomaterials* **25,** 229–238 (2004).

4. Gordon, L. M., Tran, L. & Joester, D. Atom probe tomography of apatites and bone-type mineralized tissues. *ACS Nano* **6,** 10667–10675 (2012).

5. Pleshko, N., Boskey, A & Mendelsohn, R. Novel infrared spectroscopic method for the determination of crystallinity of hydroxyapatite minerals. *Biophys. J.* **60,** 786–793 (1991).

6. Miller, L. M., Vadyasagar, V., Chance, M. R., Mendelsohn, R., Paschalis, E. P., Betts, F. & Boskey, A. L. In situ analysis of mineral content and crystallinity in bone using infrared micro-spectroscopy of the nu(4) PO(4)(3-) vibration. *Biochim. Biophys. Acta* **1527,** 11–19 (2001).

7. Paschalis, E. P., Betts, F., DiCarlo, E., Mendelsohn, R. & Boskey, A. L. FTIR microspectroscopic analysis of normal human cortical and trabecular bone. *Calcif. Tissue Int.* **61,** 480–486 (1997).

8. Uskokovic, V. The Role of Hydroxyl Channel in Defining Selected Physicochemical Peculiarities Exhibited by Hydroxyapatite. *RSC Adv.* **5,** 36614–36633 (2015).

9. Ma, G. & Liu, X. Y. Hydroxyapatite: Hexagonal or monoclinic? *Cryst. Growth Des.* **9,** 2991–2994 (2009).

10. Shepherd, J. H., Shepherd, D. V. & Best, S. M. Substituted hydroxyapatites for bone repair. *J. Mater. Sci. Mater. Med.* **23,** 2335–2347 (2012).

11. Rey, C., Combes, C., Drouet, C., Sfihi, H. & Barroug, A. Physico-chemical properties of nanocrystalline apatites: Implications for biominerals and biomaterials. *Mater. Sci. Eng. C* **27,** 198–205 (2007).

12. Liou, S. C., Chen, S. Y., Lee, H. Y. & Bow, J. S. Structural characterization of nano-sized calcium deficient apatite powders. *Biomaterials* **25,** 189–196 (2004).

13. Wu, F., Lin, D. D. W., Chang, J. H., Fischbach, C., Estroff, L. A. & Gourdon, D. Effect of the materials properties of hydroxyapatite nanoparticles on

fibronectin deposition and conformation. *Cryst. Growth Des.* **15,** 2452–2460 (2015).

14. Pathi, S. P., Lin, D. D. W., Dorvee, J. R., Estroff, L. A. & Fischbach, C. Hydroxyapatite nanoparticle-containing scaffolds for the study of breast cancer bone metastasis. *Biomaterials* **32,** 5112–5122 (2011).

15. Akkus, O., Adar, F. & Schaffler, M. B. Age-related changes in physicochemical properties of mineral crystals are related to impaired mechanical function of cortical bone. *Bone* **34,** 443–453 (2004).

16. Balasundaram, G., Sato, M. & Webster, T. J. Using hydroxyapatite nanoparticles and decreased crystallinity to promote osteoblast adhesion similar to functionalizing with RGD. *Biomaterials* **27,** 2798–2805 (2006).

17. Lin, K., Wang, X., Zhang, N. & Shen, Y. Strontium (Sr) strengthens the silicon (Si) upon osteoblast proliferation, osteogenic differentiation and angiogenic factor expression. *J. Mater. Chem. B* **4,** 24–26 (2016).

18. Boanini, E., Gazzano, M. & Bigi, A. Ionic substitutions in calcium phosphates synthesized at low temperature. *Acta Biomater.* **6,** 1882–1894 (2010).

19. Nelson, D. G. A., Coote, G. E., Vickridge, I. C. & Suckling, G. Proton microprobe determination of fluorine profiles in the enamel and dentine of erupting incisors from sheep given low and high daily doses of fluoride. *Arch. Oral Biol.* **34,** 419–429 (1989).

20. Marie, P. J., Ammann, P., Boivin, G. & Rey, C. Mechanisms of action and therapeutic potential of strontium in bone. *Calcif. Tissue Int.* **69,** 121–129 (2001).

21. Cox, R. F., Hernandez-Santana, A., Ramdass, S., McMahon, G., Harmey, J. H. & Morgan M. P. Microcalcifications in breast cancer: novel insights into the molecular mechanism and functional consequence of mammary mineralisation. *Br. J. Cancer* **106,** 525–37 (2012).

22. Sharma, T., Radosevich, J. A., Pachori, G. & Mandal, C. C. A Molecular View of Pathological Microcalcification in Breast Cancer. *J. Mammary Gland Biol. Neoplasia* **21,** 25–40 (2016).

23. Scott, R., Stone, N., Kendall, C., Geraki, K. & Rogers, K. Relationships between pathology and crystal structure in breast calcifications : an in situ X-ray diffraction study in histological sections. *Nat. Publ. Gr.* 1–6 (2016).

24. Baker, R., Rogers, K. D., Shepherd, N. & Stone, N. New relationships between breast microcalcifications and cancer. *Br. J. Cancer* **103,** 1034–9 (2010).

25. Šupová, M. Substituted hydroxyapatites for biomedical applications: A review. *Ceram. Int.* **41,** 9203–9231 (2015).

26. Webster, T. J., Massa-Schlueter, E. a., Smith, J. L. & Slamovich, E. B.

Osteoblast response to hydroxyapatite doped with divalent and trivalent cations. *Biomaterials* **25,** 2111–2121 (2004).

27. Dorozhkin, S. V. Calcium orthophosphates: occurrence, properties, biomineralization, pathological calcification and biomimetic applications. *Biomatter* **1,** 121–164 (2011).

28. Chappard, D., Bizot, P., Mabilleau, G. & Hubert, L. Aluminum and bone: Review of new clinical circumstances associated with Al3+ deposition in the calcified matrix of bone. *Morphologie* **100,** 95–105 (2015).

29. Hem, S. L. & Hogenesch, H. Relationship between physical and chemical properties of aluminum-containing adjuvants and immunopotentiation. *Expert Rev. Vaccines* **6,** 685–98 (2007).

30. Mannello, F., Tonti, G. A., Medda, V., Simone, P. & Darbre, P. D. Analysis of aluminium content and iron homeostasis in nipple aspirate fluids from healthy women and breast cancer - affected patients. *Applied Toxicology* **31,** 262–269 (2011). doi:10.1002/jat.1641

31. Mannello, F., Ligi, D. & Canale, M. Aluminium, carbonyls and cytokines in human nipple aspirate fluids: Possible relationship between inflammation, oxidative stress and breast cancer microenvironment. *J. Inorg. Biochem.* **128,** 250–256 (2013).

32. Mirick, D. K., Davis, S. & Thomas, D. B. Antiperspirant use and the risk of breast cancer. *J. Natl. Cancer Inst.* **94,** 1578–1580 (2002).

33. Degeratu, C. N., Mabilleau, G., Cincu, C. & Chappard, D. Aluminum inhibits the growth of hydroxyapatite crystals developed on a biomimetic methacrylic polymer. *J. Trace Elem. Med. Biol.* **27,** 346–351 (2013).

34. McGrath, K. G. An earlier age of breast cancer diagnosis related to more frequent use of antiperspirants/deodorants and underarm shaving. *Eur. J. Cancer Prev.* **12,** 479–485 (2003).

35. Darbre, P. D. Aluminium, antiperspirants and breast cancer. *J. Inorg. Biochem.* **99,** 1912–1919 (2005).

36. House, E., Polwart, A., Darbre, P., Barr, L., Metaxas, G. & Exley, C. The aluminium content of breast tissue taken from women with breast cancer. *J. Trace Elem. Med. Biol.* **27,** 257–266 (2013).

37. Layani, J. D., Cuisinier, F. J. G., Steuer, P., Cohen, H., Voegel, J. C. & Mayer, I. High-resolution electron microscopy study of synthetic carbonate and aluminum containing apatites. *J. Biomed. Mater. Res.* **50,** 199–207 (2000).

38. Christoffersen, J., Christoffersen, M. R., Arends, J. & Hook, M. Effect of aluminum (III) and fluoride on the demineralization of bovine enamel powder and hydroxyapatite; in vitro kinetic studies showing synergistic inhibition. *J.*

Cryst. Growth **137,** 545–552 (1994).

39. Kolekar, T. V., Thorat, N. D., Yadav, H. M., Magalad, V. T., Shinde, M. A., Bandgar, S. S., Kim, J. H. & Agawane, G. L. Nanocrystalline hydroxyapatite doped with aluminium: A potential carrier for biomedical applications. *Ceram. Int.* **42,** 5304–5311 (2016).

40. Wang, M., Wang, L., Shi, C., Sun, T., Zeng, T. & Zhu, Y. The crystal structure and chemical state of aluminum-doped hydroxyapatite by experimental and first principles calculation studies. *Phys. Chem. Chem. Phys.* **18,** 21789–21796 (2016).

41. Laurencin, D., Almora-Barrios, N., de Leeuw, N. H., Gervais, C., Bonhomme, C., Mauri, F., Chrzanowski, W., Knowles, J. C., Newport, R. J., Wong, A., Gan, Z. & Smith M. E. Magnesium incorporation into hydroxyapatite. *Biomaterials* **32,** 1826–1837 (2011).

42. Boutinguiza, M., Pou, J., Comesana, R., Lusquinos, F., de Carlos, A. & Leon, B. Biological hydroxyapatite obtained from fish bones. *Mater. Sci. Eng. C* **32,** 478–486 (2012).

43. Kunitake, J., Choi, S., Nguyen, K., Lee, M., He, F., Sudilovsky, D., Morris, P. G., Jochelson, M. S., Hudis, C. A., Muller, D. A., Fratzl, P., Fischbach, C., Masic, A. & Estroff, L. A. Correlative imgaing reveals physiochemical heterogeneity of microcalcifications in human breast carcinomas. *Submitted* (2017)

Chapter 2.

Synthesis, Characterization, and Biological Activity of Aluminum Substituted Hydroxyapatite and Amorphous Calcium Phosphate

2.1 Introduction

Hydroxyapatite (HA; $Ca_{10}(PO_4)_6(OH)_2$) is an inorganic crystalline material found in numerous hard tissues, such as bone and teeth. Biogenic HA is non-stoichiometric and is found with varying physicochemical properties (e.g., crystallinity, ionic substitutions, etc.), depending on the function and anatomy of the tissue within which the HA occurs [1–3]. Crystallinity of HA particles in bone is one of the important factors used in assessing bone quality [4–6]. Studies have shown that HA crystallinity is also an important parameter that governs various cell responses through mediating protein adsorption [7–10]. Ionic substitution in HA can also play a role in defining the function of hard tissue [2,11–15]. For example, magnesium ions were found to be localized on the grain boundaries of rodent enamel, implying functionality of wear and tear resistance of magnesium substituted HA [2]. For bone regenerative purposes, strontium substituted HA has been synthesized and shown to upregulate osteogenesis[15]. As mentioned above, physicochemical properties of HA in bone have been shown to affect and modulate the functionality of the hard tissue, which further helps us understand the importance of nanoscale characteristics of materials in bone.

HA is also found in pathological calcifications in the human body, such as cardiovascular calcification [16], dysfunctional calcified articular cartilage[17], and microcalcifications (MCs) in breast tissues [56]. In particular, MCs found in benign and

cancerous breast tissues are examined via mammograms and often used for prognosis of the disease's malignancy. With rapid growth of materials characterization technology, physicochemical information of MCs in breast tissue is more accessible and connections to pathological progressions are being made [18,19,56]. For example, Baker et al. observed correlation of carbonate content in MCs with the progression of the cancer, showing that MCs found in more invasive (malignant) tissue specimens contained less carbonate when compared to MCs found in precancerous and benign tissues [20].

Aluminum substituted HA (Al-HA) in pathological calcifications is reported in several cases: 1) accumulation of aluminum in bones of patients with renal failure[21], 2) deposition of aluminum on both cortical and trabecular region of hereditary bone tumors (exostoses)[22], 3) localization of aluminum in MCs of breast tissue of ductal carcinoma in-situ [56]. Despite the reports of Al-HA in pathological calcifications, studies of Al-HA to examine its pathological implications have not yet been reported[23–25], and only *in vitro* evaluations of Al-HA with fibroblasts have been done[23,24]. To address the paucity of knowledge in Al-HA and to understand the physicochemical properties of HA that relate to the development and progression of breast cancer, further research of Al-HA in the context of pathological calcification is necessary.

Three-dimensional (3D) poly(lactic-co-glycolic acid) (PLGA) scaffold models for cell culture have proven useful for mimicking tumor microenvironments in *in vitro* and *in vivo* studies [26–29]. The addition of HA particles to 3D polymeric scaffolds allowed for the investigation of the role of HA particles in tumor progression[8,30]. In

previous cancer studies of HA-containing PLGA scaffolds, the model was used to understand the microenvironment of bone metastasis. Considering the materials used to create this model, this model also mimics "calcified" microenvironment (e.g., MCs) found in breast tumors. To further carry out the investigation of the effects of the physicochemical properties of HA, particularly Al-HA in MCs, on tumor progression, we utilized an Al-HA particle containing PLGA scaffold model. We synthesized and characterized the particles using various techniques to understand its physicochemical properties. We further applied the particles to the PLGA scaffold system for breast cancer cell culture studies obtaining cell adsorption results showing potential of this system for cell culture studies.

2.2 Experimental

2.2.1 Particle synthesis

Particles were synthesized via an aqueous precipitation reaction of calcium nitrate ($Ca(NO_3)_2 \cdot 4H_2O$) and ammonium phosphate ($(NH_4)_2HPO_4$) [8,31]. Aluminum nitrate ($Al(NO_3)_3 \cdot 9H_2O$) was used as the aluminum source in synthesizing aluminum substituted HA (Al-HA) and aluminum substituted amorphous calcium phosphate (Al-ACP). All reagents were all obtained from Sigma-Aldrich, and all reagents were used as received. De-ionized water (18.2 MΩ) was used for all aqueous solutions. For HA synthesis, a 250 mL solution of ammonium phosphate was added to a 250 mL solution of calcium nitrate under rapid stirring at room temperature. The final molarity of calcium and phosphate was 5 mM and 3 mM, respectively, with a 500mL reaction volume, to achieve calcium to phosphate ratio of 1.67. Prior to mixing, the pH of all

solution was adjusted to pH 9.5 using concentrated ammonium hydroxide (NH_4OH; 28~30wt%). After mixing, the precipitates were aged in 65 ^{0}C oven for 20 hours. For aluminum substituted HA synthesis, all parameters and procedures were kept the same as the HA synthesis except for addition of aluminum nitrate in calcium solution to obtain a final concentrations ranging from 0.1 mM to 1 mM of Al^{3+} ions. For Al-HA and Al-ACP, the Al^{3+} concentration is 0.45 mM and 0.9 mM, respectively. After 20 hours of aging, particles were collected via centrifugation (Thermos Scientific Sorvall Legend RT + Centrifuge, 3600 g, 5 min). Collected pellets of particles were triple washed by 0.15 M ammonium hydroxide and lyophilized for 72 hours to obtain dry particles.

See Appendices 1-5 and 7 for additional synthetic conditions and results.

2.2.2 Particle characterization

Particles were characterized by scanning electron microscopy (SEM) and transmission electron microscopy (TEM) for shape and morphology. Powder x-ray diffraction (pXRD), and Fourier transform infrared (FTIR) were used for obtaining information on material phase, crystallinity, and local ordering. Induced coupled plasma – atomic emission spectroscopy (ICP-AES) was used to analyze elemental composition of the synthesized particles. X-ray photoelectron spectroscopy (XPS) was used to qualitatively identify surface elemental composition of the particles.

Particles were aliquoted from the final washing step on to a silicon wafer and carbon coated for examination under SEM (Tescan Mira3 FESEM, 5 keV). For TEM, particles were dispersed in pure ethanol (200 proof) and dropped onto a carbon-coated

copper TEM grid (Electron Microscopy Sciences) and examined by bright-field TEM (FEI Tecnai T-12 Spirit, 80 keV). Dried particles were characterized via pXRD (Scintag Inc. PAD-X theta-theta X-ray Diffractometer, Cu Kα 1.54 Å, accelerating voltage 40 keV, current 40 mA, step-scan, 1.5 deg/min). Particle sizes were determined from full width-half max of (002) peak of hydroxyapatite ($2\Theta = 25.88^0$) by applying the Scherrer equation using an Al_2O_3 standard (JADE 9 software, Materials Data, Inc.). KBr pellets were prepared for FTIR (Bruker Hyperion FT-IR Spectrometer, 2 cm^{-1} resolution, 64 scans) spectra scans. 200mg of FTIR-grade KBr particles (Sigma-Aldrich) and 2 mg of synthesized particles were mixed and cold-pressed in to pellets. Particle crystallinities were obtained from the peak splitting factor proposed by Weiner and Bar-Yosef [32] normalizing summation of two absorbance maxima at 562 cm^{-1} and 602 cm^{-1} to the minimum between the two maxima. For XPS, photoemission spectra for elemental analysis were acquired using a Surface Science Instruments SSX-100 with operating pressure of ~2*10-9 Torr. Monochromatic Al K-alpha x-rays (1486.6 eV) were used with beam diameter of 1 mm. Photoelectrons were collected at a 55˚ emission angle. A hemispherical analyzer determined electron kinetic energy, using a pass energy of 150 V. A flood gun was used for charge neutralization because samples were insulating. For ICP-AES, particles were digested in 5% nitric acid prior to analysis.

See Appendix 6 for Raman characterization of the particles.

2.2.3 Scaffold fabrication

3D porous particle containing PLGA scaffolds were fabricated via gas-foaming/particulate leaching methods previously described in the literature[8,27,30]. Briefly, 4 mg of PLGA particles (Lakeshore Biomaterials, ground and sieved, average diameter 250 μm), 4 mg of PLGA microspheres (synthesized via double emulsion process, diameter 5~50 μm), 8 mg of synthesized particles (HA, Al-HA, Al-ACP), and 152 mg of NaCl (JT Baker, sieved to diameter of ~250 μm) were mixed well and cold-pressed under 2 metric tons in a Carver Press (Fred S. Carver Inc.) for 1 minute. Pressed pellets (8 mm diameter, 2 mm thickness) were pressurized in a pressure vessel (Parr Instruments 4677) under 800 psi of carbon dioxide gas for 18 hours, followed by rapid release of pressure resulting in foaming of polymer matrix. Foamed scaffolds were submerged in DI-H_2O for 24 hours to leach out porogenic NaCl particles. Blank PLGA scaffolds were fabricated with the identical parameters and procedures mentioned above with the exception of synthetic particle addition. All scaffolds were sterilized in 70% ethanol for 30 minutes and triple-washed in sterile PBS prior to cell culture. See Appendix 8 for additional details.

2.2.4 Scaffold characterization

Particle exposure to the surfaces of the scaffold pores were initially assessed with Alizarin Red staining (VWR Life Science). Scaffolds were immersed in 40 mM Alizarin Red staining working solution at room temperature on orbital shaker for 20 minutes. Scaffolds were then removed and washed with DI water twice and dried prior to imaging (Appendix 11).

Particle morphology and distribution on pore surfaces of the scaffolds were characterized via SEM (LEO 1550, 2kV). Scaffolds were freeze-fractured under liquid nitrogen to expose the pores in the central parts of the scaffolds and mounted on aluminum SEM stubs (Electron Microscopy Sciences) with carbon tape. Samples were subsequently sputter coated using Iridium target. Pore surfaces distant from fractured spots were imaged with SEM to best represent the surfaces interacting with cells. See Appendix 8 for additional characterization of particles in scaffold.

2.2.5 Cell culture and characterization of tumor cell adhesion behavior

Human MDA-MB231 breast cancer cells (ATCC) were incubated under standard culture conditions (37 ^{0}C, 5% CO_2) in 10% FBS (Tissue Culture Biologicals) supplemented DMEM (Invitrogen) and 1% penicillin/streptomycin (Invitrogen) for 3 days. For initial cell adhesion studies, sterilized and washed scaffolds were seeded with 1.5 million MDA-MB231 cells and subsequently maintained under dynamic culture condition on an orbital shaker up to 30 min and non-adhering cells were washed with 1mL PBS. PBS used for washing was collected to count and calculate number of adhered cells using Bright Line Counting Chamber (Hausser Scientific). To measure initial DNA quantity, incubated scaffolds were doubly washed in 1mL PBS and lysed in Caron's buffer by sonication. Centrifugation of lysate and scaffold debris were done to collect supernatant DNA content for quantification (QuantiFluor dsDNA System, Promega Corporation).

2.2.6 Statistical analysis

One-way ANOVA and Student's t-test were used to determine statistical significance among conditions. Tukey's post-hoc test was used for pairwise significance analysis. Significance between the groups and the blank scaffold, HA scaffold, and Al-HA scaffold are denoted by (*), (#), and (●), respectively. For all pairwise analysis, $p<0.05$ is indicated by single symbol and $p<0.01$ is indicated by double symbols. Cell culture experiments were done in triplicates or more for all conditions. Result data are presented as a mean with error bars representing standard deviations.

2.3 Results

2.3.1 Particle synthesis and Characterization

HA particles were synthesized via a co-precipitation method in aqueous media. To investigate the effect of aluminum substitution in HA, increments of aluminum ion concentrations were used in the individual Al-substituted HA syntheses. As aluminum concentration was increased in the reaction, we observed morphological changes of the resulting particles through electron microscopy. The HA particles have a round ended rod-like morphology (Fig. 2.1A) with an average dimension of 50 nm in length and 25 nm in width (Fig. 2.1B). Increasing the concentration of aluminum in Al-substituted HAs showed a gradual increase in the aspect ratio of the particles (Fig. 2.1C,D; see Appendix 1 for data for lower concentrations). Further increase in the aluminum concentration resulted in the appearance of a new particle morphology in addition to the elongated needle-like particles. We started observing spherical particles together with needle-shaped particles above 0.7 mM aluminum concentration in the synthesis (data not shown). The population of spherical particles increased as

aluminum concentration was further increased from 0.7 mM. From 0.9 mM aluminum concentration and above, we obtained a homogeneous population of spherical particles in the synthesis (Fig. 2.1E,F), which were later confirmed to be amorphous particles through pXRD (Fig. 2.2) and FTIR (Fig. 2.3). Based on the uniformity of phase and morphologies present, particles synthesized with 0 mM, 0.45 mM, and 0.9 mM aluminum ion concentrations (HA, Al-HA, and Al-ACP respectively) were selected for cell studies.

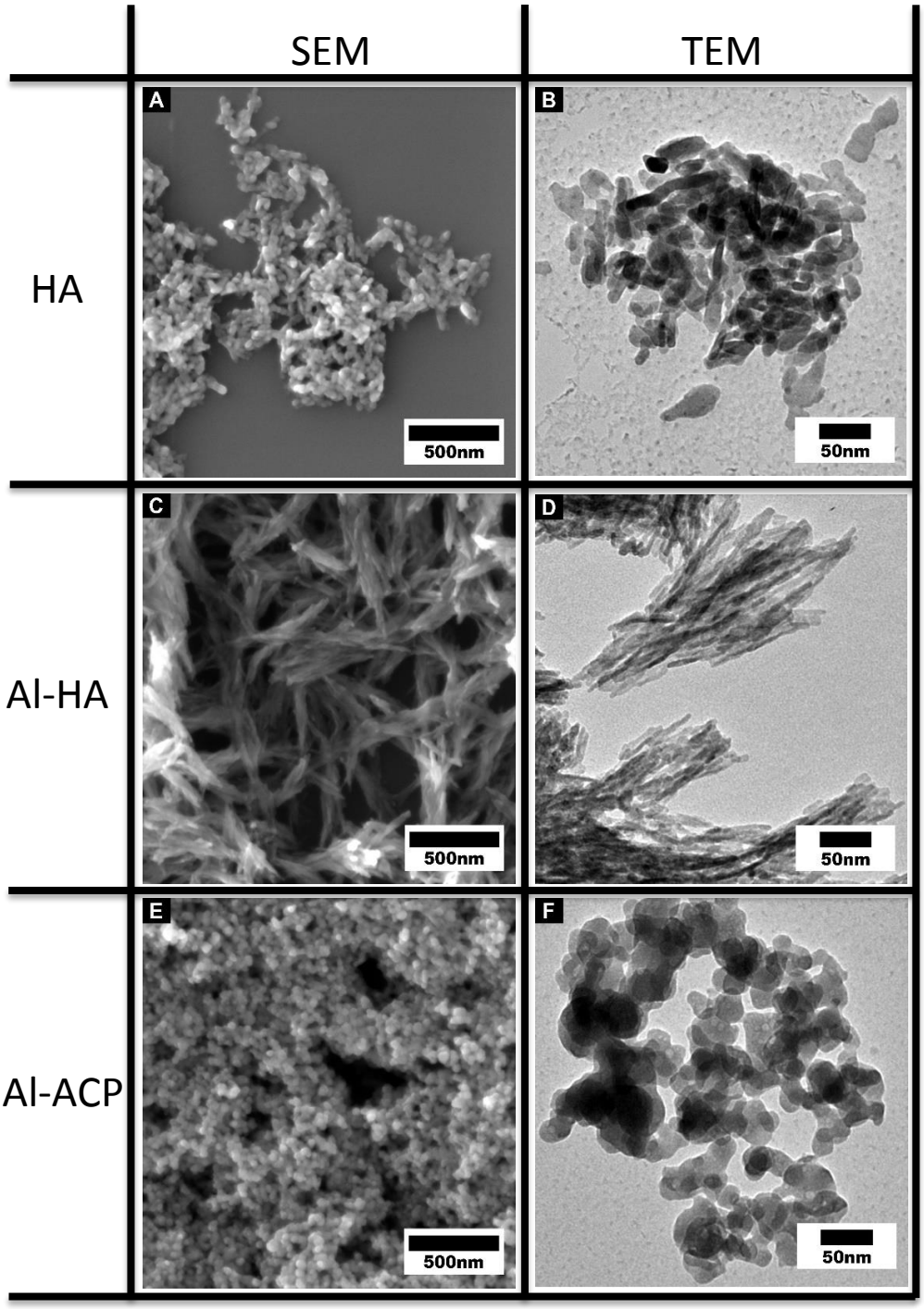

Figure 2.1. Electron microscopy (SEM and TEM) images of nanoparticles with varying concentrations of Aluminum. Hydroxyapatite (HA) nanoparticles (A, B); Aluminum substituted hydroxyapatite (Al-HA) nanoparticles (C, D); Aluminum substituted amorphous calcium phosphate (Al-ACP) nanoparticles (E, F)

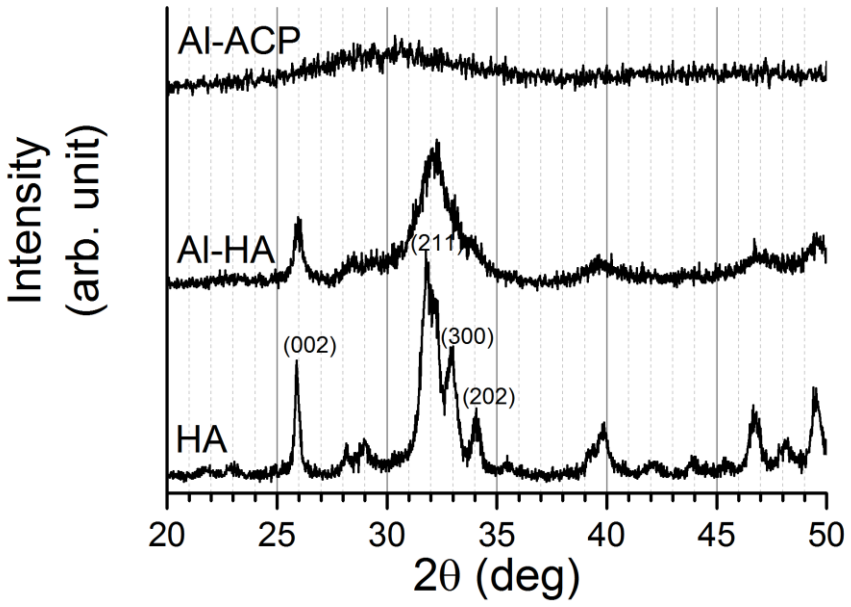

Figure 2.2. Powder XRD of HA, Al-HA, and Al-ACP particles. Main HA peaks are indexed. (Hydroxyapatite; PDF#00-009-0432)

We confirmed the phase of the HA and Al-HA particles as hydroxyapatite from pXRD characterization (Fig. 2.2). Broadening of pXRD characteristic peaks of hydroxyapatite were observed as the concentration of aluminum was increased in the synthesis, indicating aluminum inclusion in the crystallization process decreased the crystallinity of particles. The characteristic peaks of HA are present in the Al-HA pXRD pattern, indicating that the hydroxyapatite structure is still maintained with aluminum inclusion in the structure. In Al-ACP pXRD pattern, a broad band around $2\Theta = 30^{0}$ was observed indicating that Al-ACP particles do not have any long-range order indicative of a crystalline material. Scherrer analysis was done on the (002) peak ($2\Theta = 25.8^{0}$) to calculate crystal domain size of synthetic particles (Table 2.1). The (002) peak was selected for calculation because of its resolution (i.e., no neighboring

characteristic peaks overlap) and its representation of the c-axis in crystal structure. Based on the Scherrer analysis, HA particles have an average domain size of 33.5 nm and Al-HA particles have a domain size of 16.2 nm.

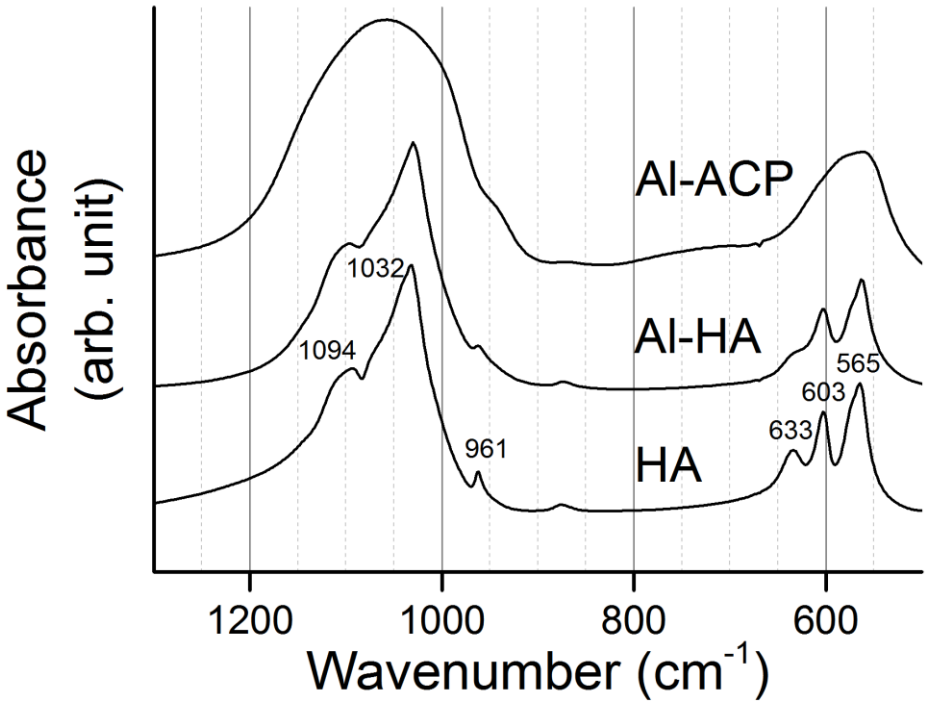

Figure 2.3. FTIR spectrum of HA, Al-HA, Al-ACP particles. ν4 PO_4 mode (565, 603 cm^{-1}), ν1 PO_4 mode (961 cm^{-1}), ν3 PO_4 mode (1032, 1094 cm^{-1}) and OH liberation mode (633 cm^{-1}) are labeled.

FTIR spectroscopy was used to assess the structure and chemistry of the synthetic particles (Fig. 2.3). Two peaks at 565 and 603 cm^{-1}, corresponding to the asymmetric bending modes of phosphate (ν4 phosphate mode), are well resolved in HA and Al-HA spectra, indicating the apatitic character of the two synthetic particles [33]. The peak splitting factor of these ν4 phosphate peaks are also parameters used to assess the crystallinity of hydroxyapatites [1,32]. The difference of the peak splitting factor between HA and Al-HA corroborates the difference in crystallinity

observed in pXRD result (Table 2.1). The hydroxide liberation peak at 633 cm^{-1} is observed in crystalline HAs, and the presence of this well-resolved peak in the HA spectrum indicates the synthetic hydroxyapatite character of hydroxide's cationic environment [34,35]. For Al-ACP, no separation of ν4 phosphate peaks and hydroxide liberation peak were observed, indicating Al-ACP does not have apatitic structure and it is in a more disordered state, further confirming the broad band observed in pXRD that shows that Al-ACP is amorphous (Fig. 2.2; Al-ACP). Peaks at 1032 and 1094 cm^{-1} are attributed to ν3 phosphate mode in hydroxyapatite, and these peaks are resolved in HA and Al-HA spectra. Similar to ν4 phosphate mode in Al-ACP, ν1 and ν3 phosphate modes are not resolved as peaks, rather shown as a broad band between 950 and 1200 cm^{-1}, indicating its amorphous state. The maxima of broad band in ν3 phosphate mode of Al-ACP is shifted to a higher wavenumber, suggesting the presence of acid phosphate in the structure[34].

XPS was used to qualitatively characterize the surfaces of the particles. We collected spectra of Al2p for each particle conditions (Fig. 2.4). XPS is a surface sensitive characterization technique, and its probing depth is 1~2 nm from the surface. Al-HA samples had no prominent peak in the Al2p binding energy region, indicating that either the aluminum is at a concentration lower than the detection limit of XPS or the surface of Al-HA particles were absent of aluminum species. Al-ACP particles showed a prominent peak in the Al2p binding energy region, indicating presence of aluminum species on the surfaces of the particles.

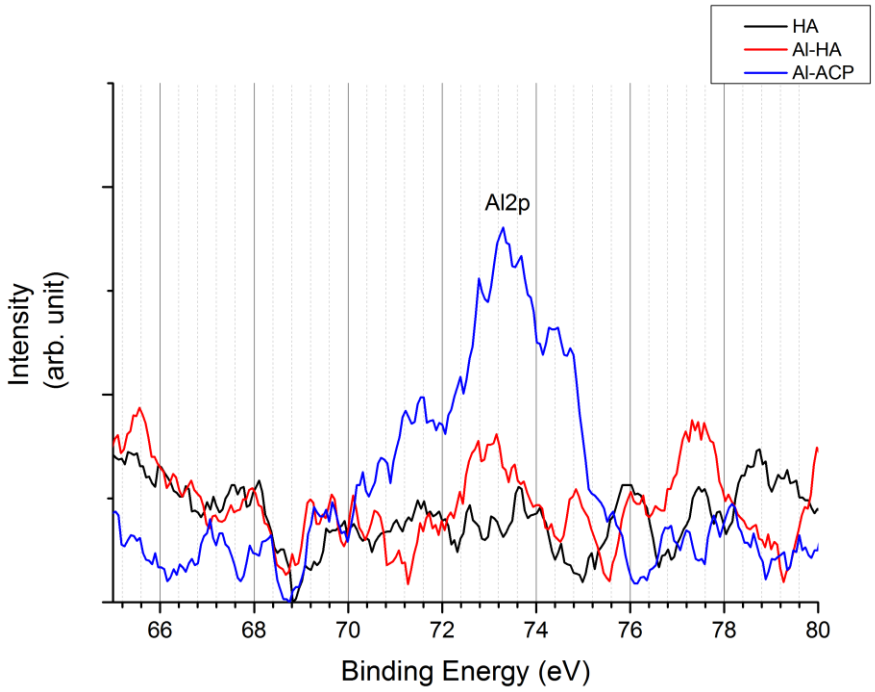

Figure 2.4. XPS spectra of HA (black), Al-HA (red), and Al-ACP (blue) on Al2p binding energy (70~78 eV) region. HA and Al-HA showed no prominent detection of aluminum in the particles, whereas Al-ACP shows a distinct peak at 73.6 eV indicating presence of aluminum on the surface of particles (1~2 nm depth from surface).

Quantitative elemental analysis of synthesized particles was done by ICP-AES. ICP-AES analysis confirmed that aluminum was incorporated in the particles (Table 2.1), further implying that incorporation of aluminum in the particle formation resulted in changes in particle morphology and crystallinity. Ca/P ratio was used to indirectly assign the phase of particles. Biogenic HA tends to have a wide range of Ca/P ratio of 1.61~1.71. ACP has even wider Ca/P ratio range, from 1.2~2.2[36,37]. Considering the computational result from a different study [23], we calculated both Ca^{2+} and Al^{3+} cations for the (Ca+Al)/P ratio of our synthesized particles, and the ratio was well in the range of reported ratios for HA and ACP.

Table 2.1. Elemental composition (wt%), (Ca+Al)/P ratio, Scherrer calculation, dimension, and peak splitting factor of synthesized HA, Al-HA, and Al-ACP.

	Ca (wt%)	P (wt%)	Al (wt%)	Ca/P	(Ca+Al)/P	(002) Scherrer (nm)	Size in TEM (nm)	Peak Splitting factor (FTIR)
HA	35.99	15.94	0.01	1.74	1.74	33.5	L 50 x W 25	4.9
Al-HA	31.41	14.69	0.66	1.65	1.70	16.2	L 100 x W 15	4.03
Al-ACP	27.53	14.84	2.74	1.49	1.64	-	D 50	-

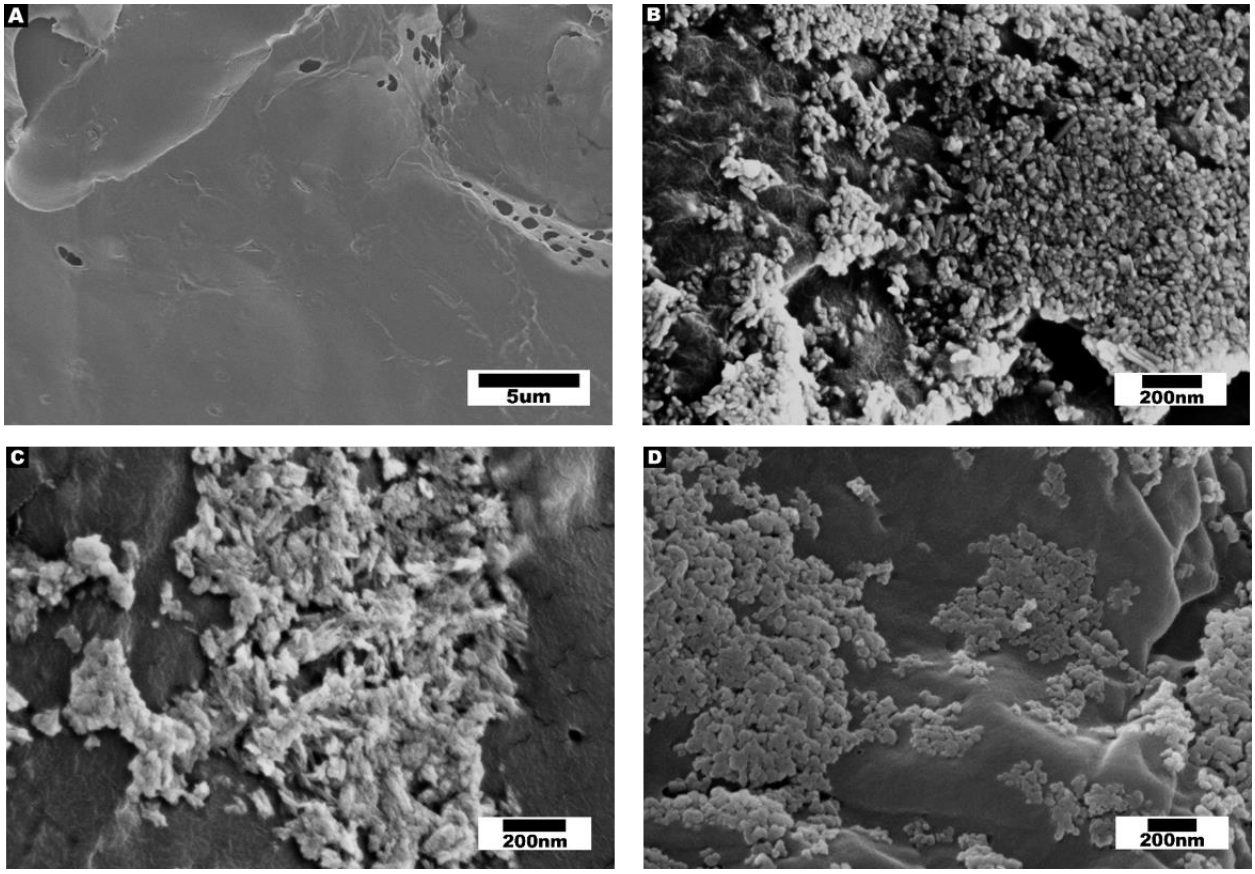

Figure 2.5. High magnifications of scaffold pore surfaces. Blank PLGA scaffold pore surface (A), HA scaffold pore surface (B), Al-HA scaffold pore surface (C), Al-ACP scaffold pore surface (D).

2.3.2 Scaffold characterization

A 3D PLGA porous scaffold with two levels of pore size was fabricated via the particulate leaching and gas foaming techniques. Addition of synthesized particles to the PLGA scaffolds did not show significant alterations of scaffold's microstructure (i.e. wall thickness and pore sizes). Large pores, average diameter of 250 μm, are formed from NaCl particulate leaching of the scaffold, whereas small pores, average diameter of 10 μm (SEM; see Appendix 8 for additional details of scaffold characterization.), are formed via gas foaming method. Different levels of open pores in the scaffolds were designed to increase interconnectivity of the pores and increase mechanical stability throughout the scaffold network [38].

For initial macroscopic confirmation of particle exposure to the pore surfaces, Alizarin Red staining was done to show the accessibility of particles for cell interaction (AR staining; Appendix 11). SEM imaging of the scaffold pore surface further showed exposed particles accessible for cell interactions (Fig. 2.5). HA, Al-HA, and Al-ACP particles maintained their morphology (rod-like, needle-like, and spherical morphology, respectively, data not shown) throughout the scaffold fabrication process of pellet pressing, CO_2 pressurizing, and particulate leaching. Regions of dense and sparse particle distributions throughout the pores were observed, and similar particle surface coverage was also observed between different scaffolds.

2.3.3 Effect of aluminum substituted particles on MDA-MB231 adhesion

To determine relevance between breast cancer cells and aluminum incorporated MCs, *in vitro* cell culturing experiments were done by seeding MDA-

MB231 malignant breast cancer cells into prepared scaffolds. Both cell adhesion propensity and DNA quantity at 0 hour between blank-scaffold and HA-scaffold conditions confirmed the preference of cells to adhere to HA compared to bare PLGA surfaces [8,30]. Similar to the previous findings on lower crystalline HA promoting better cell adhesion, Al-HA-scaffolds had the highest cell adhesion compared to the more crystalline HA-scaffold. However, Al-ACP-scaffolds showed the lowest cell adhesion compared to the other two particle-containing scaffolds (Fig. 2.6). The Al-ACP-scaffold's result is contradictory to previous reports on crystallinity of HA and cell adhesion trend [8], considering Al-ACP particles' amorphous nature as an extreme end-point in terms of crystallinity range.

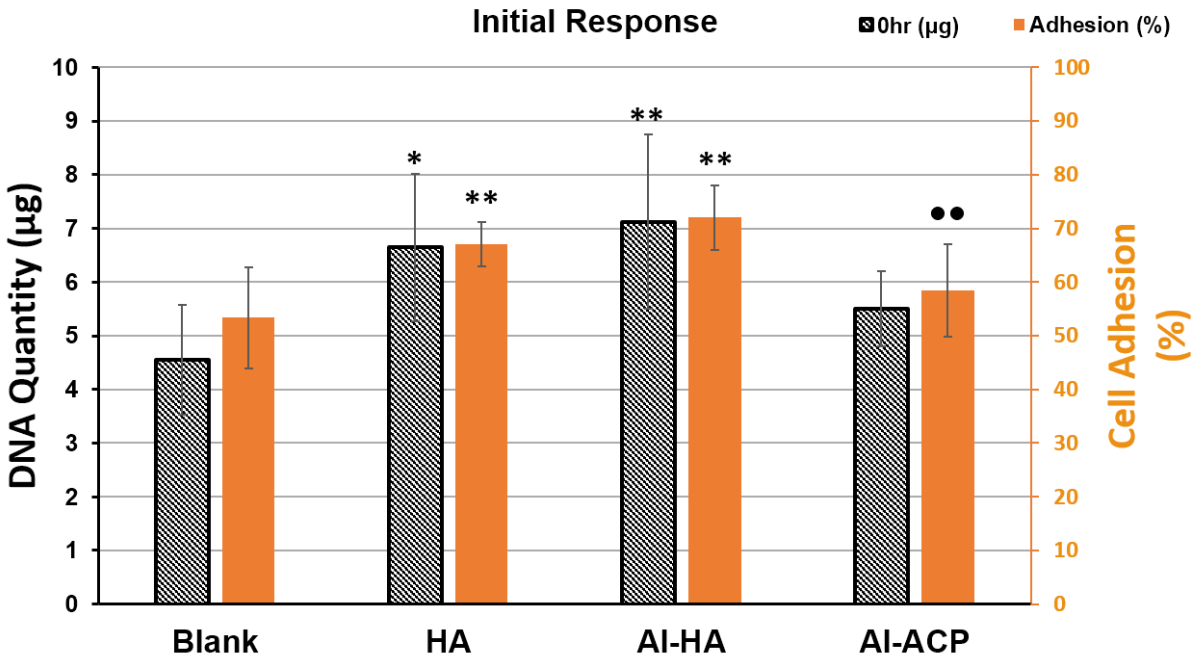

Figure 2.6. MDA-MB231 cell adhesion onto Blank, HA-, Al-HA-, and Al-ACP-scaffolds as quantified via QuantiFluor DNA assay of cell lysates 0.5 hrs after seeding (in black oblique). Percentage of cells adhering to the scaffolds from initial cell seeding (1.5mil cells) quantified by Bright Line Counting Chamber (in orange). Significance between groups and Blank-, HA-, Al-HA-, and Al-ACP-scaffolds are denoted by (*), (○), and (●) respectively. In all cases, $p < 0.05$ is denoted by single symbol and $p < 0.01$ is denoted by double symbols.

2.4 Discussion

To better understand cellular response to biogenic Al-HA, a study on the *in vitro* synthesis of aluminum substituted HA with biological relevance was conducted. Previously, syntheses of aluminum substituted HA have been investigated[23,24,31,39,40], but these methods were not aimed to produce HA with the chemistry, size, and crystallinity of biogenic HA. We modified a previously reported [8] aqueous synthesis procedure of obtaining HA particles of biological relevance for our aluminum substituted HA synthesis. Extensive characterizations (XRD, FTIR, SEM, TEM, ICP, and XPS) of our particles showed that HA, Al-HA, and Al-ACP fell under the range of biogenic particle size and crystallinity. Peak broadening present in pXRD data suggests a decrease in particle size and crystallinity as aluminum is added to the HA synthesis. The peak splitting factor and peak broadening of phosphate modes in FTIR data showed local symmetry of phosphate species in particles was also decreasing with the inclusion of aluminum. ICP-AES data confirmed that the particles contained calcium, phosphorous, and aluminum (in Al-HA and Al-ACP). XPS data further showed that aluminum is detected only on the surfaces of Al-ACP.

3D culture systems for studying tumor microenvironment are methods designed to better reflect the *in vivo* tumor behavior in *in vitro* tumor cell cultures[41]. *In vitro* 3D PLGA scaffold culture system instigates "3D" tumor formation, reflecting complex microenvironment of tumors, such as tumor growth profiles and nutrient depletion inherent in cores of tumor tissues[29]. Addition of HA particles in the PLGA scaffold fabrication enables tumors to be studied in in-vitro bone analogs[8,30,42,43], and

this system can also be used to investigate cell/tissue response in other calcified environment, such as MCs found in breast lesions in this study. By utilizing this platform we were able to study an *in vitro* model of MCs and its correlation to breast cancer progression. PLGA polymer is not readily degraded and does not contain natural adhesion sites, such as integrin binding arginine-glycine-aspartic acid (RGD) peptides, allowing us to observe primarily the effects of different particles added to the system as MC analogs. And through changing the physicochemistry of the particles (specifically inclusion of aluminum in HA in this study), we were able to see how breast cancer cells respond to different chemistry of calcified microenvironment.

Cell adhesion is followed by adsorption of media protein to material surfaces. The extent and the strength of protein adsorption often drives the biomaterial's bio-activity (e.g. proliferation by activating signaling components of adhesion plaques) [44,45]. Abnormal upregulation of proliferation is one of the hallmarks of cancer that marks the pathology's malignancy[46]. Understanding breast cancer cell's proliferation signaling through adhesion to HA (found in MCs) is an approach to correlating malignancy of breast cancer to the presence of MCs in the tumor microenvironment. Thus, investigating cell adhesion modulated by the physicochemical properties of HA in MC is an important first step in evaluating progression of breast cancer.

Previous studies showed that the physicochemical properties, specifically the crystallinity of HA particles, are highly relevant to propensity of protein adsorption and conformation upon adsorption on particle surfaces [7]. In a study done by Wu et al., [7] less crystalline HA particles showed more negative surface charge (zeta-potential)

resulting in stronger electrostatic interactions with proteins. From this electrostatic interaction, less crystalline HA particles were shown to adsorb more protein compared to high crystalline HA particles [7]. Furthermore, quantity and quality of protein adsorption on the surfaces of biomaterials mainly dictates cell adhesion propensity. Based on these reports, our results on blank-, HA-, and Al-HA-scaffold cell adhesion correspond to the proposed surface charge model, but not for the Al-ACP-scaffold. We were expecting to see the highest cell adhesion from Al-ACP-scaffold, given its amorphous nature, but we observed the lowest cell adhesion (Fig. 2.6). The amorphous structure of Al-ACP is expected to have more negative charges exposed on the surface, because of the disordered assembly of ions. These ions would be expected to increase protein adsorption and available integrin binding sites for cell adhesion. This crystallinity and surface charge model was only applicable to HA- and Al-HA-scaffold's cell adhesion data, requiring alternative parameter, Al^{3+}, to be included in explaining the Al-ACP-scaffold's cell adhesion result.

On the particle surface of Al-ACP, the aluminum may take part in forming ionic complexes that neutralize the surface charge of the particles, which further leads to a lower amount of protein adsorption and to less cell adhesion compared with the HA and Al-HA particles. Wavellite ($Al_3(PO_4)_2(OH)_2 \cdot 5H_2O$) is an aluminum phosphate mineral found in earth's crust, and geological wavellite's electrokinetic properties (i.e., surface charge) and chemistry have been characterized[47]. Wavellite's abundance in Al^{3+} results in various ionic aluminum species (Al^{3+}, $Al(OH)_2^+$, $Al(OH)^{2+}$, and $Al(OH)_4^-$) that participate in lowering negative surface charge when compared to geologic HA[47,48]. Surface sensitive XPS analysis (Fig. 2.4) shows that Al-ACP

contains aluminum species on the surface of the particles, which further indicates that these aluminum species will actively be involved in creating more positive (i.e., less negative) surface charge. In comparison to Al-ACP, Al-HA was shown to contain no or undetectable amounts of aluminum species on the particle surface according to XPS data. This XPS result suggests that the increase in surface charge due to crystallinity dominates the cell adhesion mechanism (initially via protein adsorption) in HA and Al-HA, where at higher aluminum concentrations, Al-ACP, the effect of ionic aluminum species on the surface dominate the cellular adhesion mechanism. Thus, we propose ionic incorporations in calcium phosphate particles, along with crystallinity, as a guiding factor for cell adhesion.

2.5 Conclusion

We fabricated HA, Al-HA, and Al-ACP particles in a cell-culture system that mimics the microenvironments of calcified tissues, particularly in this work as MCs of breast cancer lesions. By incorporating aluminum in the particles, we were able to conduct *in vitro* assessment reflecting recent findings of aluminum incorporation in HA in the context of breast cancer [56]. Aluminum inclusion in HA results in a decrease in crystallinity and changes in morphology from a round, rod-like into a thinner, needle-like morphology when compared to pure HA. Further inclusion of aluminum results in formation of spherical Al-ACP particles. In our cell studies of MDA-MB231, we found that the Al-HA scaffold induced a similar amount of cell adhesion compared to the HA scaffold. Whereas, the Al-ACP scaffold induced relatively less cell adhesion compared to HA scaffold. Our Al-ACP scaffold system shows the least

amount of cell adhesion, which is in disagreement with previous reports, suggesting chemistry of calcium phosphate particles, along with crystallinity, play a role in cell adhesion. First principle calculations of aluminum substituted HA show aluminum is substituting in the Ca(II) site of the HA crystal [23]. Further characterization techniques such as X-ray absorption spectroscopy utilizing synchrotron radiation sources will be necessary to experimentally validate substitution sites and oxidation states of aluminum in HA for our system. Although specific substitution sites and its implications to cell responses were unknown, characterizations performed here were sufficient to categorize particles to be biologically relevant. This research lays the groundwork for future studies to investigate the role of Al-HA in breast cancer diagnosis and prognosis.

2.6 References

1. Asscher, Y., Weiner, S. & Boaretto, E. Variations in atomic disorder in biogenic carbonate hydroxyapatite using the infrared spectrum grinding curve method. *Adv. Funct. Mater.* **21,** 3308–3313 (2011).

2. Gordon, L. M., Tran, L. & Joester, D. Atom probe tomography of apatites and bone-type mineralized tissues. *ACS Nano* **6,** 10667–10675 (2012).

3. Pasteris, J. D., Wopenka, B., Freeman, J. J., Rogers, K., VAlsoami-Jones, E., van der Houwen J. A. M. & Silva, M. J. Lack of OH in nanocrystalline apatite as a function of degree of atomic order: Implications for bone and biomaterials. *Biomaterials* **25,** 229–238 (2004).

4. Pleshko, N., Boskey, A. & Mendelsohn, R. Novel infrared spectroscopic method for the determination of crystallinity of hydroxyapatite minerals. *Biophys. J.* **60,** 786–793 (1991).

5. Miller, L. M., Vairavamurthy, V., Chance, M. R., Mendelsohn, R., Pashcalis, E. P., Betts, F. & Boskey, A. L. In situ analysis of mineral content and crystallinity in bone using infrared micro-spectroscopy of the nu(4) PO(4)(3-) vibration. *Biochim. Biophys. Acta* **1527,** 11–19 (2001).

6. Paschalis, E. P., Betts, F., DiCarlo, E., Mendelsohn, R. & Boskey, A. L. FTIR microspectroscopic analysis of normal human cortical and trabecular bone. *Calcif. Tissue Int.* **61,** 480–486 (1997).

7. Wu, F., Lin, D. D. W., Chang, J. H., Fischbach, C., Estroff, L. A. & Gourdon, D. Effect of the materials properties of hydroxyapatite nanoparticles on fibronectin deposition and conformation. *Cryst. Growth Des.* **15,** 2452–2460 (2015).

8. Pathi, S. P., Lin, D. D. W., Dorvee, J. R., Estroff, L. A. & Fischbach, C. Hydroxyapatite nanoparticle-containing scaffolds for the study of breast cancer bone metastasis. *Biomaterials* **32,** 5112–5122 (2011).

9. Akkus, O., Adar, F. & Schaffler, M. B. Age-related changes in physicochemical properties of mineral crystals are related to impaired mechanical function of cortical bone. *Bone* **34,** 443–453 (2004).

10. Balasundaram, G., Sato, M. & Webster, T. J. Using hydroxyapatite nanoparticles and decreased crystallinity to promote osteoblast adhesion similar to functionalizing with RGD. *Biomaterials* **27,** 2798–2805 (2006).

11. Shepherd, J. H., Shepherd, D. V. & Best, S. M. Substituted hydroxyapatites for bone repair. *J. Mater. Sci. Mater. Med.* **23,** 2335–2347 (2012).

12. Lin, K., Wang, X., Zhang, N. & Shen, Y. Strontium (Sr) strengthens the silicon (Si) upon osteoblast proliferation, osteogenic differentiation and angiogenic factor expression. *J. Mater. Chem. B* **4,** 24–26 (2016).

13. Boanini, E., Gazzano, M. & Bigi, a. Ionic substitutions in calcium phosphates synthesized at low temperature. *Acta Biomater.* **6,** 1882–1894 (2010).

14. Nelson, D. G. A., Coote, G. E., Vickridge, I. C. & Suckling, G. Proton microprobe determination of fluorine profiles in the enamel and dentine of erupting incisors from sheep given low and high daily doses of fluoride. *Arch. Oral Biol.* **34,** 419–429 (1989).

15. Marie, P. J., Ammann, P., Boivin, G. & Rey, C. Mechanisms of action and therapeutic potential of strontium in bone. *Calcif. Tissue Int.* **69,** 121–129 (2001).

16. Bertazzo, S., Gentleman, E., Cloyd, K. L., Chester, A. H., Yacoub, M. H. & Stevens, M. M. Nano-analytical electron microscopy reveals fundamental insights into human cardiovascular tissue calcification. *Nat. Mater.* **12,** 576–83 (2013).

17. Fuerst, M., Lammers, L., Schafer, F., Niggemeyer, O., Steinhagen, J., Lohmann, C. H. & Ruther, W. Investigation of calcium crystals in OA knees. *Rheumatol. Int.* **30,** 623–631 (2010).

18. Cox, R. F., Hernandez-Santana, A., Ramdass, S., McMahon, G., Harmey, J. H. & Morgan, M. P. Microcalcifications in breast cancer: novel insights into the molecular mechanism and functional consequence of mammary mineralisation. *Br. J. Cancer* **106,** 525–37 (2012).

19. Sharma, T., Radosevich, J. A., Pachori, G. & Mandal, C. C. A Molecular View of Pathological Microcalcification in Breast Cancer. *J. Mammary Gland Biol. Neoplasia* **21,** 25–40 (2016).

20. Baker, R., Rogers, K. D., Shepherd, N. & Stone, N. New relationships between breast microcalcifications and cancer. *Br. J. Cancer* **103,** 1034–9 (2010).

21. Parsons V, D. C., Goode C, Ogg C & Siddiqui J. Aluminium in bone from patients with renal failure. *Br. Med. J.* **4,** 273–275 (1971).

22. Chappard, D., Mabilleau, G., Moukoko, D., Henric, N., Steiger, V., Le Nay, P., Frin, J. M. & De Bodman, C. Aluminum and iron can be deposited in the calcified matrix of bone exostoses. *J. Inorg. Biochem.* **152,** 174–179 (2015).

23. Wang, M., Wang, L., Shi, C., Sun, T., Zeng, Y. & Zhu, Y. The crystal structure and chemical state of aluminum-doped hydroxyapatite by experimental and first principles calculation studies. *Phys. Chem. Chem. Phys.* **18,** 21789–21796 (2016).

24. Kolekar, T. V., Thorat, N. D., Yadav, H. M., Magalad, V. T., Shinde, M. A., Bandgar, S. S., Kim, J. H. & Agawane, G. L. Nanocrystalline hydroxyapatite doped with aluminium: A potential carrier for biomedical applications. *Ceram. Int.* **42,** 5304–5311 (2016).

25. Kandori, K., Toshima, S., Wakamura, M., Fukusumi, M. & Morisada, Y. Effects of modification of calcium hydroxyapatites by trivalent metal ions on the protein adsorption behavior. *J. Phys. Chem. B* **114,** 2399–2404 (2010).

26. Balachander, G. M., Balaji, S. A., Rangarajan, A. & Chatterjee, K. Enhanced Metastatic Potential in a 3D Tissue Scaffold toward a Comprehensive in Vitro Model for Breast Cancer Metastasis. *ACS Appl. Mater. Interfaces* **7,** 27810–27822 (2015).

27. Lynch, M. E. *et al.* In vivo tibial compression decreases osteolysis and tumor formation in a human metastatic breast cancer model. *J. Bone Miner. Res.* **28,** 2357–2367 (2013).

28. Lynch, M. E., Chiou, A. E., Lee, M. J., Marcott, S. C., Polamraju, P. V., Lee, Y. & Fischbach, C. Three-Dimensional Mechanical Loading Modulates the Osteogenic Response of Mesenchymal Stem Cells to Tumor-Derived Soluble Signals. *Tissue Eng. Part A* **22,** 1006–1015 (2016).

29. Fischbach, C., Chen, R., Matsumoto, T., Schmelzle, T., Brugge, J. S., Polverini, P. J. & Mooney, D. J. Engineering tumors with 3D scaffolds. *Nat. Methods* **4,** 855–860 (2007).

30. Pathi, S. P., Kowalczewski, C., Tadipatri, R. & Fischbach, C. A novel 3-D mineralized tumor model to study breast cancer bone metastasis. *PLoS One* **5,** 1–10 (2010).

31. Wakamura, M., Kandori, K. & Ishikawa, T. Surface structure and composition of calcium hydroxyapatites substituted with Al(III), La(III) and Fe(III) ions. *Colloids Surfaces A Physicochem. Eng. Asp.* **164,** 297–305 (2000).

32. Weiner, S. & Bar-Yosef, O. States of preservation of bones from prehistoric sites in the Near East: A survey. *J. Archaeol. Sci.* **17,** 187–196 (1990).

33. Rey, C., Shimizu, M., Collins, B. & Glimcher, M. J. Resolution-enhanced Fourier transform infrared spectroscopy study of the environment of phosphate ions in the early deposits od a solid phase of calcium phosphate in bone and enamel, and their evolution with age. I: investigations in the n4PO4 domain. *Calcif. Tissue Int.* **46,** 384–394 (1990).

34. Rey, C., Maran, O., COmbes, C., Brouet, C., Grossin, D. & Sarda, S. Characterization of calcium phosphates using vibrational spectroscipies. Bennissan, B. (ed.) *Advances in Calcium Phosphate Biomaterials*. *Livro* **2,** (2014).

35. Rey, C., Combes, C., Drouet, C. & Glimcher, M. J. Bone mineral: Update on chemical composition and structure. *Osteoporos. Int.* **20,** 1013–1021 (2009).

36. Dorozhkin, S. V. Calcium orthophosphates: occurrence, properties, biomineralization, pathological calcification and biomimetic applications. *Biomatter* **1,** 121–164 (2011).

37. Dorozhkin, S. V. Amorphous calcium (ortho)phosphates. *Acta Biomater.* **6,** 4457–4475 (2010).

38. Sheridan, M. H., Shea, L. D., Peters, M. C. & Mooney, D. J. Bioabsorbable polymer scaffolds for tissue engineering capable of sustained growth factor delivery. **64,** 91–102 (2000).

39. Mayer, I. Synthesis, characterization and high temperature analysis of Al-containing hydroxyapatites. *J. Cryst. Growth* **172,** 219–225 (1997).

40. Zhang, C., Zhang, X., Liu, C., Sun, K. & Yuan, J. Nano-alumina/hydroxyapatite composite powders prepared by in-situ chemical precipitation. *Ceram. Int.* **42,** 279–285 (2015).

41. Pampaloni, F., Reynaud, E. G. & Stelzer, E. H. K. The third dimension bridges the gap between cell culture and live tissue. *Nat. Rev. Mol. Cell Biol.* **8,** 839–845 (2007).

42. Murphy, W. L., Kohn, D. H. & Mooney, D. J. Growth of bone-like mineral within porous poly(lactide-co-glycolide) scaffolds in vitro. *J. Biomed. Mater. Res.* **50,** 50–58 (2000).

43. Murphy, W. L., Peters, M. C., Kohn, D. H. & Mooney, D. J. Sustained release of vascular endothelial growth factor from mineralized poly(lactide-co-glycolide) scaffolds for tissue engineering. *Biomaterials* **21,** 2521–2527 (2000).

44. Bacakova, L., Filova, E., Parizek, M., Ruml, T. & Svorcik, V. Modulation of cell adhesion, proliferation and differentiation on materials designed for body implants. *Biotechnol. Adv.* **29,** 739–767 (2011).

45. Playford, M. P. & Schaller, M. D. The interplay between Src and integrins in normal and tumor biology. *Oncogene* **23,** 7928–7946 (2004).

46. Hanahan, D. & Weinberg, R. A. The hallmarks of cancer. *Cell* **100,** 57–70 (2000).

47. Nunes, A. P. L., Peres, A. E. C., de Araujo, A. C. & Valadão, G. E. S. Electrokinetic properties of wavellite and its floatability with cationic and anionic collectors. *J. Colloid Interface Sci.* **361,** 632–638 (2011).

48. Vučinić, D. R., Radulović, D. S. & Deušić, S. D. Electrokinetic properties of hydroxyapatite under flotation conditions. *J. Colloid Interface Sci.* **343,** 239–245 (2010).

49. Chappard, D., Bizot, P., Mabilleau, G. & Hubert, L. Aluminum and bone: Review of new clinical circumstances associated with Al3+ deposition in the calcified matrix of bone. *Morphologie* **100,** 95–105 (2015).

50. Kiss, T., Zatta, P. F. & Corain, B. Interaction of aluminium (III) with phosphate-binding sites: biological aspects and implications. *Coord. Chem. Rev.* **149,** 329–346 (1996).

51. Berthon, G. Aluminium speciation in relation to aluminium bioavailability, metabolism and toxicity. *Coord. Chem. Rev.* **228,** 319–341 (2002).

52. Mannello, F., Tonti, G. A., Medda, V., Simone, P. & Darbre, P. D. Analysis of aluminium content and iron homeostasis in nipple aspirate fl uids from healthy women and breast cancer - affected patients. 262–269 (2011). doi:10.1002/jat.1641

53. Mannello, F., Ligi, D. & Canale, M. Aluminium, carbonyls and cytokines in human nipple aspirate fluids: Possible relationship between inflammation, oxidative stress and breast cancer microenvironment. *J. Inorg. Biochem.* **128,** 250–256 (2013).

54. House, E., Polwart, A., Darbre, P., Barr, L., Metaxas, G. & Exley, C. The aluminium content of breast tissue taken from women with breast cancer. *J. Trace Elem. Med. Biol.* **27,** 257–266 (2013).

55. Rodrigues-Peres, R. M., Cadore, S., Febraio, S., Heinrich, J. K., Serra, K. P., Derchain, S. F. M. & Sarian, L. O. Aluminum concentrations in central and peripheral areas of malignant breast lesions do not differ from those in normal breast tissues. *BMC Cancer* **13,** 104 (2013).

56. Kunitake, J., Choi, S., Nguyen, K., Lee, M., He, F., Sudilovsky, D., Morris, P. G., Jochelson, M. S., Hudis, C. A., Muller, D. A., Fratzl, P., Fischbach, C., Masic, A. & Estroff, L. A. Correlative imgaing reveals physiochemical heterogeneity of microcalcifications in human breast carcinomas. *Submitted* (2017)

Chapter 3.

Conclusion and Future Works

3.1 Conclusion and future works

The aims of this thesis were to synthesize biologically relevant Al-HA particles, characterize the physicochemical properties of these materials, and begin to understand the role of Al-HA in breast cancer pathology and progression. I developed an aqueous co-precipitation method to synthesize Al-HA with controlled amount of aluminum substitution. Various characterization techniques such as pXRD, vibrational spectroscopy (FTIR and Raman), electron microscopy (SEM and TEM), and XPS were used. From electron microscopy, I found that with increasing concentration of aluminum, particle morphologies change from round-ended rod-like shape to more thinner and elongated needle-like shape. Further increase of aluminum resulted in formation of amorphous particles (Al-ACP). From pXRD and vibrational spectroscopy, I found that aluminum inhibits crystallization of HA and induces decrease in long-range order and local ordering of the crystal. From XPS data, it was determined that aluminum species were localized in the bulk of Al-HA particles, whereas Al-ACP had aluminum species on the surface and in the bulk of particles. However, with the available characterization techniques, the aluminum's substitution site in the HA structure was not accessible. Due to lack of crystallinity in the Al-HA and Al-ACP particles, techniques utilizing structural probes available for non-crystalline and highly disordered materials, such as x-ray absorption spectroscopy, is required. Despite the lack of atomic scale characterization and understanding of Al-

HA, I obtained sufficient information to conclude that the synthetic materials (HA, Al-HA, and Al-ACP) are biologically relevant and therefore proceeded to apply the materials for breast cancer cell studies.

To understand the pathological role of Al-HA involved MCs found in breast tissue, I adopted a 3D porous PLGA scaffold cell culture system for *in vitro* cell culture experiments. MDA-MB231 cells were seeded and cultured to assess cell adhesion on different materials conditions. I found out that cells adhere better on Al-HA-scaffolds compared to HA-scaffolds, whereas less adhesion on Al-ACP-scaffolds were observed. Based on work done by Wu et al., less crystalline HA showed more negative electrostatic interactions with proteins, which results in favorable surface modifications (i.e. more protein adsorption) for cell adhesion [1]. Adopting the results of Wu et al., I propose that scaffolds containing lower crystalline Al-HA resulted in higher cell adhesion. I further hypothesized that relatively aluminum rich surfaces of Al-ACP particles resulted in positive increase of surface charge creating unfavorable adhesion surfaces for cells. To further validate this hypothesis, careful measurement of surface charge (zeta-potential) of the Al-HA and Al-ACP particles is required.

Determination of cell adhesion propensity depending on our cell adhesion study suggests Al-HA involved MC microenvironment may lead to increased growth of tumor cells. Activation of focal adhesion plaques (assembly of adhesion related biomolecules initiated by adhesion receptors) depending on the strength of cell adhesion plays a role in cell growth and cell activity [2,3]. To further venture into breast cancer cell adhesion results from this thesis, observation of adhered cell morphology through microscopy is suggested to indirectly validate cell surface interactions to Al-

HA and Al-ACP. Investigations of other cancer cell lines and malignancies can also provide insight into cell-specific responses to these mineral particles, see Appendix 10 for preliminary results using a different cell line.

SEM, XRD, and Alizarin Red staining data of our scaffold system showed that scaffold surfaces have particles with properties that of freshly synthesized particles. However, I encountered difficulty in obtaining consistent results of cell growth and secretions of soluble factors from multiple 72 hour cell culture experiments (see Appendix 9 for preliminary results). To understand the cause of inconsistency and to optimize longer cell culture experiment, further characterization of scaffolds and optimization of cell seeding procedure is required. Measurements of pore sizes and its distribution, investigating cell seeding conditions, and culturing different breast cancer cell line may be of interest in further optimizing this experimental system.

Results from this thesis have laid down the groundwork to better understand the MC's materials properties and its connections to breast cancer. I hope that further application of different materials, different breast cancer cells, and different culture condition help us achieve deeper understanding of the pathological connections to MCs and how microenvironments of breast tumor have effect in cancer progression.

3.2 References

1. Wu, F. *et al.* Effect of the materials properties of hydroxyapatite nanoparticles on fibronectin deposition and conformation. *Cryst. Growth Des.* **15,** 2452–2460 (2015).

2. Bacakova, L., Filova, E., Parizek, M., Ruml, T. & Svorcik, V. Modulation of cell adhesion, proliferation and differentiation on materials designed for body implants. *Biotechnol. Adv.* **29,** 739–767 (2011).

3. Playford, M. P. & Schaller, M. D. The interplay between Src and integrins in normal and tumor biology. *Oncogene* **23,** 7928–7946 (2004).

Appendix 1

Aluminum Substituted Hydroxyapatite Synthesis Optimization

A.1.1. Particle Synthesis

i. Post-mix pH adjustment / Ammonia (x1), DI Water (x2) Washing / Ambient Drying

Particles were synthesized via an aqueous precipitation reaction of calcium salt and phosphate salt [1,2]. Aluminum nitrate ($Al(NO_3)_3 \cdot 9H_2O$) was used as the aluminum source in synthesizing aluminum substituted HA (Al-HA) and aluminum substituted amorphous calcium phosphate (Al-ACP). $Ca(NO_3)_2 \cdot 4H_2O$, $(NH_4)_2HPO_4$, and $Al(NO_3)_3 \cdot 9H_2O$ were all obtained from Sigma-Aldrich, and all reagents were used as received. De-ionized water (18.2 MΩ) was used for all aqueous solutions. For HA synthesis, a 250 mL solution of $(NH_4)_2HPO_4$ was added to a 250 mL solution of $Ca(NO_3)_2 \cdot 4H_2O$ under rapid stirring at room temperature. The final molarity of calcium and phosphate was 5 mM and 3 mM, respectively, with a 500mL reaction volume, to achieve calcium to phosphate ratio of 1.67. Right after mixing, the pH of the solution was adjusted to 9.5 using concentrated NH_4OH (28~30wt%). After pH adjustment, the precipitates were aged in 65^0C oven for 20 hours. For aluminum substituted HA synthesis, all parameters and procedures were kept the same as the HA synthesis except for addition of $Al(NO_3)_3 \cdot 9H_2O$ in calcium solution to obtain a final concentrations ranging from 0.1 mM to 1 mM of Al^{3+} ions. After 20 hours of aging, particles were collected via centrifugation (Thermos Scientific Sorvall Legend RT + Centrifuge, 3600 g, 5 min). Collected pellets of particles were washed with 0.15 M

NH_4OH once, and with DI water twice. Washed and centrifuged pellets were dried under ambient condition for 72 hrs.

ii. Pre-mix pH adjustment / Ammonia (x3) Washing / Lyophilization

Particles were synthesized via an aqueous precipitation reaction of calcium salt and phosphate salt [1,2]. Aluminum nitrate ($Al(NO_3)_3 \cdot 9H_2O$) was used as the aluminum source in synthesizing aluminum substituted HA (Al-HA) and aluminum substituted amorphous calcium phosphate (Al-ACP). $Ca(NO_3)_2 \cdot 4H_2O$, $(NH_4)_2HPO_4$, and $Al(NO_3)_3 \cdot 9H_2O$ were all obtained from Sigma-Aldrich, and all reagents were used as received. De-ionized water (18.2 MΩ) was used for all aqueous solutions. For HA synthesis, a 250 mL solution of $(NH_4)_2HPO_4$ was added to a 250 mL solution of $Ca(NO_3)_2 \cdot 4H_2O$ under rapid stirring at room temperature. The final molarity of calcium and phosphate was 5 mM and 3 mM, respectively, with a 500mL reaction volume, to achieve calcium to phosphate ratio of 1.67. Prior to mixing, the pH of all solutions were adjusted to 9.5 using concentrated NH_4OH (28~30wt%). After mixing, the precipitates were aged in 65^0C oven for 20 hours. For aluminum substituted HA synthesis, all parameters and procedures were kept the same as the HA synthesis except for addition of $Al(NO_3)_3 \cdot 9H_2O$ in calcium solution to obtain a final concentrations ranging from 0.1mM to 1mM of Al^{3+} ions. After 20 hours of aging, particles were collected via centrifugation (Thermos Scientific Sorvall Legend RT + Centrifuge, 3600 g, 5 min). Collected pellets of particles were washed with 0.15 M NH_4OH three times. Washed and centrifuged pellets were lyophilized for 72 hours to obtain dry particles.

A.1.2. Particle Characterization

Particles were characterized by scanning electron microscopy (SEM) for shape and morphology. Powder x-ray diffraction (pXRD) was used for obtaining information on material phase and crystallinity.

Particles were aliquoted from the final washing step on to a silicon wafer and carbon coated for examination under SEM (Tescan Mira3 FESEM, 5kV). Dried particles were characterized via pXRD (Scintag Inc. PAD-X theta-theta X-ray Diffractometer, Cu Kα 1.54Å, accelerating voltage 40kV, current 40mA, step-scan, 1.5 deg/min).

A.1.3. Solution chemistry calculation

Visual MINTEQ 3.1 was used to calculate and hypothesize the solution chemistry between two reaction conditions. To calculate the reacting chemical (ionic) species in calcium and aluminum solution prior to mixing, parameters of pH 6.5 and pH 9.5 in room temperature were determined for 5 mM Ca^{2+} and 0.45 mM Al^{3+} aqueous solutions. Also, in addition to calcium and aluminum, 3 mM phosphate was also added in the calculation to also predict the ionic species in the reaction vessels.

A.1.3. Results

SEM data for both post-mix and pre-mix pH adjustment procedures, shows that particle becomes elongated and thinner as the aluminum concentration is increased in the synthesis. Also, at high concentrations of aluminum, different particle

morphology (sphere-shape) appears in the product along with the needle-shaped particles. One thing to notice is that the concentration of aluminum for the initial appearance of sphere-shaped particles is different from post-mix and pre-mix pH adjustments. Both XRD data shows the decrease of crystallinity for these two procedures.

The pH of solutions for post-mix procedure was in the range of 6.0 to 6.7, and for pre-mix procedure was in the range of 9.1 to 9.3. Aluminum concentration of 0.45mM for both procedures were used for Visual MINTEQ 3.1 calculation and pH of 6.5 and 9.5 for post-mix and pre-mix, respectively.

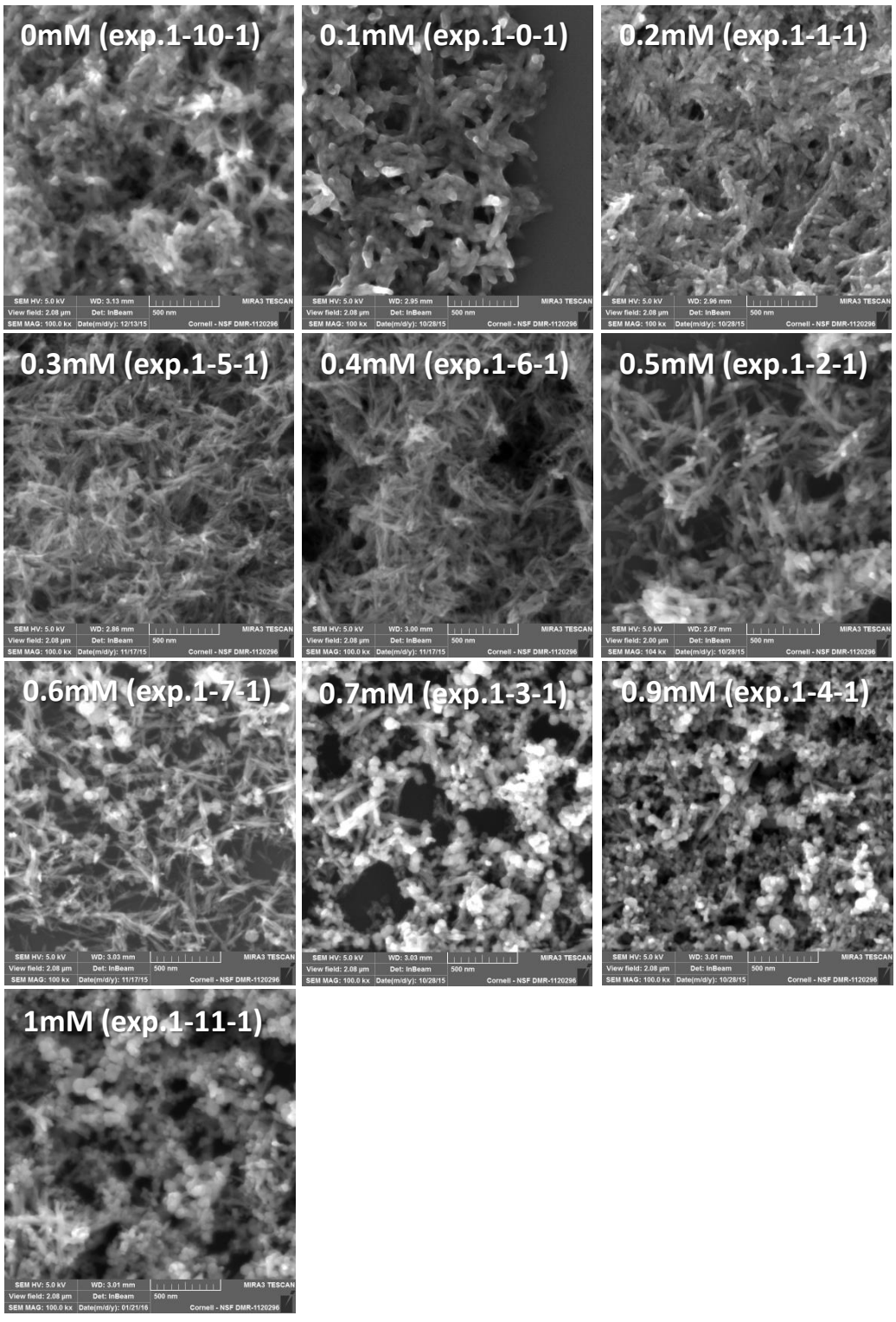

Figure A.1-1. SEM images of post-mix pH adjusted particles with different concentrations of aluminum

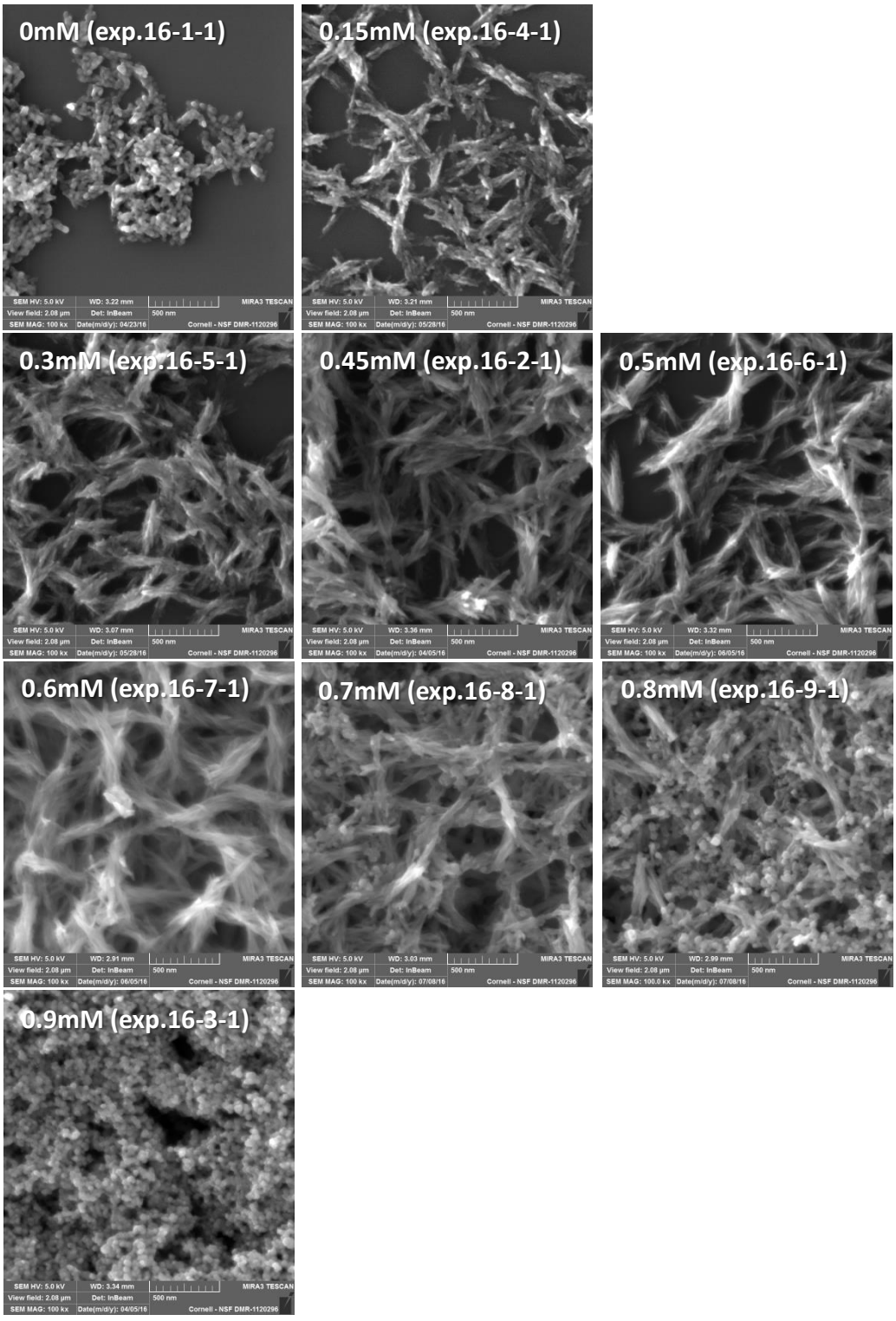

Figure A.1-2. SEM images of pre-mix pH adjusted particles with different concentrations of aluminum

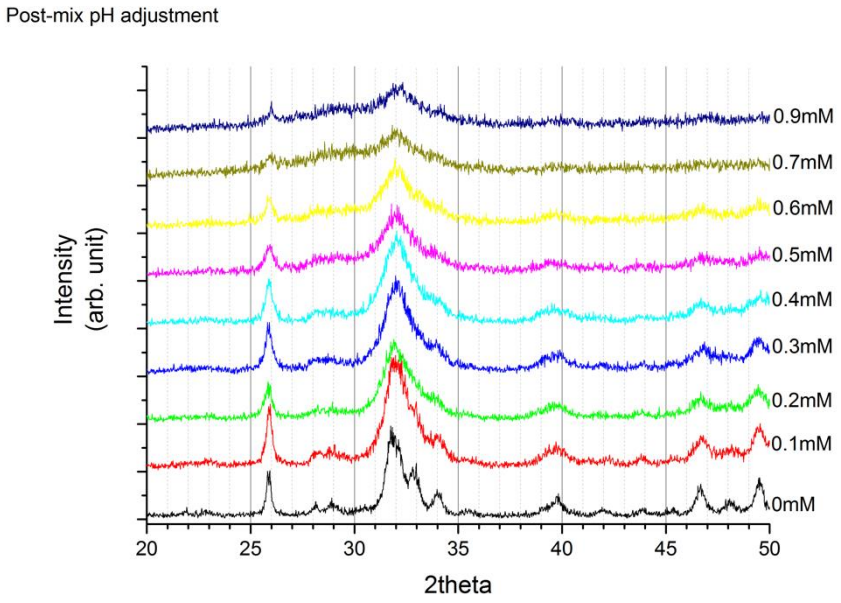

Figure A.1-3. XRD of post-mix pH adjusted particles with different concentrations of aluminum

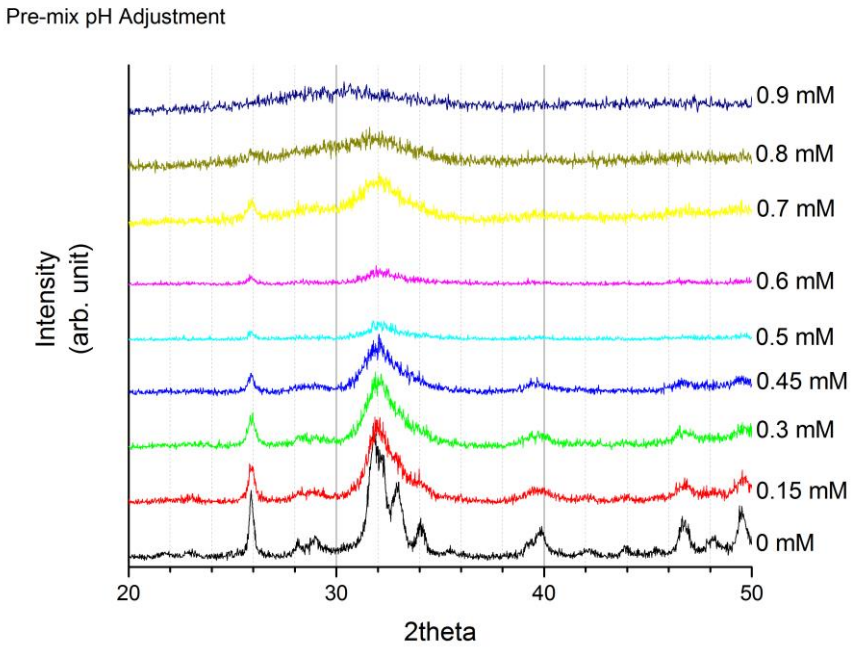

Figure A.1-4. XRD of pre-mix pH adjusted particles with different concentrations of aluminum

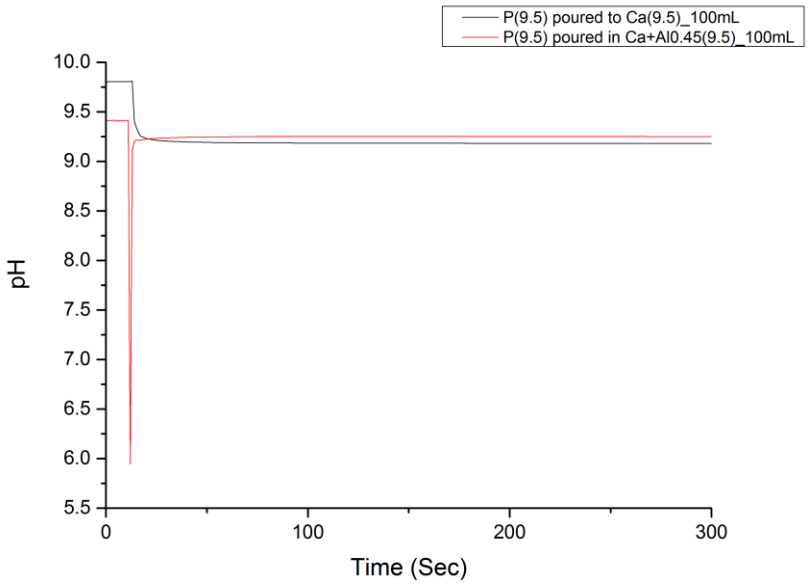

Figure A.1-5. Real time pH measurement of precipitation reactions of HA and Al-HA (0.45 mM)

Table A.1-1. Visual MINTEQ 3.1 data of calcium (5 mM) and aluminum (0.45mM) in pH 6.5 and pH 9.5 aqueous solution. Ionic species in different pH conditions are shown in the table. Difference in aluminum species depending on pH implies different reaction may occur upon introduction of phosphate ions for precipitation reaction.

pH 6.5	Al and Ca only; species		
	Component	% of total concentration	Species name
	Ca+2	100	Ca+2
	Al+3	0.108	Al+3
		0.08	Al3(OH)4+5
		0.017	Al2(OH)2+4
		2.039	AlOH+2
		23.803	Al(OH)2+
		27.121	Al(OH)3 (aq)
		46.832	Al(OH)4-
pH 9.5			
	Component	% of total concentration	Species name
	Ca+2	99.954	Ca+2
		0.046	CaOH+
	Al+3	0.058	Al(OH)3 (aq)
		99.942	Al(OH)4-

Appendix 2

Aluminum Substituted Hydroxyapatite Synthesis at Lower pH

A.2.1. Particle Synthesis

i. No pH adjustment / Ammonia (x1), DI Water (x2) Washing / Ambient Drying

Particles were synthesized via an aqueous precipitation reaction of calcium salt and phosphate salt [1,2]. Aluminum nitrate ($Al(NO_3)_3 \cdot 9H_2O$) was used as the aluminum source in synthesizing aluminum substituted HA (Al-HA) and aluminum substituted amorphous calcium phosphate (Al-ACP). $Ca(NO_3)_2 \cdot 4H_2O$, $(NH_4)_2HPO_4$, and $Al(NO_3)_3 \cdot 9H_2O$ were all obtained from Sigma-Aldrich, and all reagents were used as received. De-ionized water (18.2 MΩ) was used for all aqueous solutions. For HA synthesis, a 250 mL solution of $(NH_4)_2HPO_4$ was added to a 250 mL solution of $Ca(NO_3)_2 \cdot 4H_2O$ under rapid stirring at room temperature. The final molarity of calcium and phosphate was 5 mM and 3 mM, respectively, with a 500mL reaction volume, to achieve calcium to phosphate ratio of 1.67. After mixing, the precipitates were aged in 65^0C oven for 20 hours. For aluminum substituted HA synthesis, all parameters and procedures were kept the same as the HA synthesis except for addition of $Al(NO_3)_3 \cdot 9H_2O$ in calcium solution to obtain a final concentrations of 0.45 mM and 0.9 mM of Al^{3+} ions. After 20 hours of aging, particles were collected via centrifugation (Thermos Scientific Sorvall Legend RT + Centrifuge, 3600g, 5min). Collected pellets of particles were washed with 0.15 M NH_4OH once, and with DI water twice. Washed and centrifuged pellets were dried under ambient condition for 72 hrs.

ii. pH adjustment to 6.5 / Ammonia (x3) Washing / Lyophilization

Particles were synthesized via an aqueous precipitation reaction of calcium salt and phosphate salt [1,2]. Aluminum nitrate ($Al(NO_3)_3 \cdot 9H_2O$) was used as the aluminum source in synthesizing aluminum substituted HA (Al-HA) and aluminum substituted amorphous calcium phosphate (Al-ACP). $Ca(NO_3)_2 \cdot 4H_2O$, $(NH_4)_2HPO_4$, and $Al(NO_3)_3 \cdot 9H_2O$ were all obtained from Sigma-Aldrich, and all reagents were used as received. De-ionized water (18.2 MΩ) was used for all aqueous solutions. For HA synthesis, a 250 mL solution of $(NH_4)_2HPO_4$ was added to a 250 mL solution of $Ca(NO_3)_2 \cdot 4H_2O$ under rapid stirring at room temperature. The final molarity of calcium and phosphate was 5 mM and 3 mM, respectively, with a 500mL reaction volume, to achieve calcium to phosphate ratio of 1.67. Prior to mixing, the pH of all solutions were adjusted to 6.5 using either concentrated NH_4OH (28~30wt%) or 5 % HNO_3. After mixing, the precipitates were aged in 65^0C oven for 20 hours. For aluminum substituted HA synthesis, all parameters and procedures were kept the same as the HA synthesis except for addition of $Al(NO_3)_3 \cdot 9H_2O$ in calcium solution to obtain a final concentrations of 0.45 mM of Al^{3+} ions. After 20 hours of aging, particles were collected via centrifugation (Thermos Scientific Sorvall Legend RT + Centrifuge, 3600g, 5min). Collected pellets of particles were washed with 0.15 M NH_4OH three times. Washed and centrifuged pellets were lyophilized for 72 hours to obtain dry particles.

A.2.2 Particle characterization

Powder x-ray diffraction (pXRD) was used for obtaining information on material phase and crystallinity. Dried particles were characterized via pXRD (Scintag Inc. PAD-X theta-theta X-ray Diffractometer, Cu Kα 1.54Å, accelerating voltage 40kV, current 40mA, step-scan, 1.5 deg/min).

A.2.3. Results

Low pH synthesis was conducted to understand how pH effects particle formation and its morphologies. As concentration of aluminum was increased, pH of mixed solutions became lower. And with pH of mixed solution lower than 6.5, we observed formation of octacalcium phosphate (OCP) as the result of syntheses.

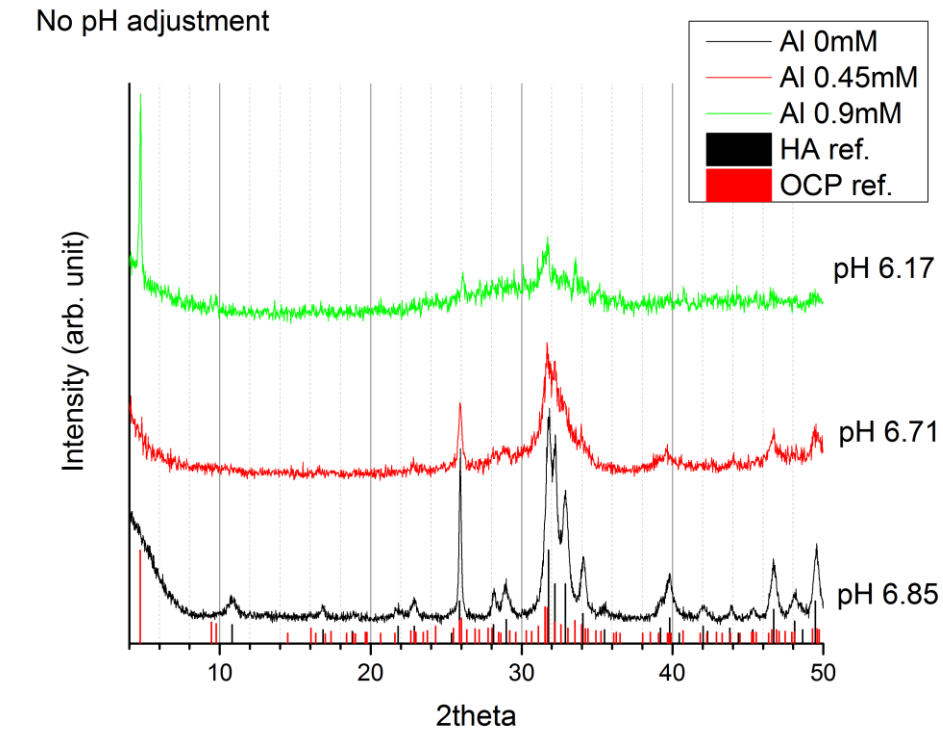

Figure A.2-1. Powder XRD data for particle synthesis without pH adjustments.

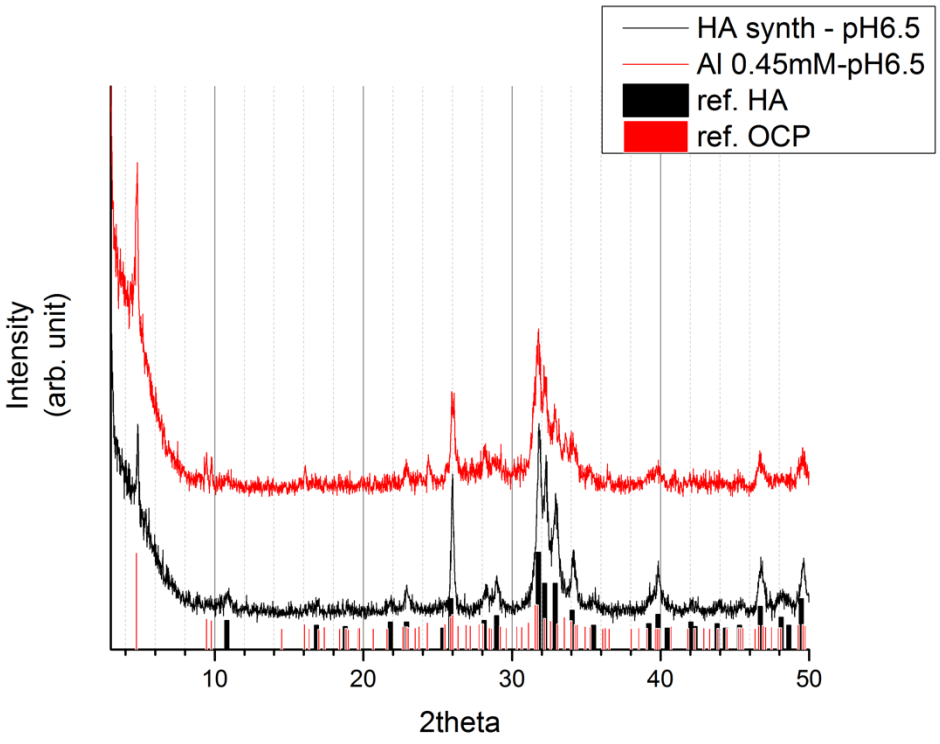

Figure A.2-2. Powder XRD data for particle synthesis with pH adjustment to 6.5.

Appendix 3

Aluminum Substituted Hydroxyapatite Using Aluminate for Aluminum Source

A.3.1. Particle Synthesis

Post-mix pH adjustment / Ammonia (x3) Washing / Lyophilization

Particles were synthesized via an aqueous precipitation reaction of calcium salt and phosphate salt [1,2]. Sodium aluminate ($Na_2O{\cdot}Al_2O_3$) was used as the aluminum source in synthesizing aluminum substituted HA (AlO2-HA) and aluminum substituted amorphous calcium phosphate (Al-ACP). $Ca(NO_3)_2{\cdot}4H_2O$, $(NH_4)_2HPO_4$, and $Na_2O{\cdot}Al_2O_3$ were all obtained from Sigma-Aldrich, and all reagents were used as received. De-ionized water (18.2 MΩ) was used for all aqueous solutions. For HA synthesis, a 250 mL solution of $(NH_4)_2HPO_4$ was added to a 250 mL solution of $Ca(NO_3)_2{\cdot}4H_2O$ under rapid stirring at room temperature. The final molarity of calcium and phosphate was 5 mM and 3 mM, respectively, with a 500mL reaction volume, to achieve calcium to phosphate ratio of 1.67. Right after mixing, the pH of the solution was adjusted to 9.5 using concentrated NH_4OH (28~30wt%). After pH adjustment, the precipitates were aged in 65^0C oven for 20 hours. For aluminum substituted HA synthesis, all parameters and procedures were kept the same as the HA synthesis except for addition of $Na_2O{\cdot}Al_2O_3$ in calcium solution to obtain a final concentrations 0.45, 0.9, and 1.2 mM of AlO_2^- ions. After 20 hours of aging, particles were collected via centrifugation (Thermos Scientific Sorvall Legend RT + Centrifuge, 3600g, 5min). Collected pellets of particles were washed with 0.15 M

NH_4OH three times. Washed and centrifuged pellets were lyophilized for 72 hours to obtain dry particles.

A.3.2. Particle Characterization

Particles were characterized by scanning electron microscopy (SEM) for shape and morphology. Powder x-ray diffraction (pXRD) was used for obtaining information on material phase and crystallinity. Raman and Fourier Transform Infra-Red spectroscopy were used for chemical analysis.

Particles were aliquoted from the final washing step on to a silicon wafer and carbon coated for examination under SEM (Tescan Mira3 FESEM, 5kV). Dried particles were characterized via pXRD (Scintag Inc. PAD-X theta-theta X-ray Diffractometer, Cu Kα 1.54Å, accelerating voltage 40kV, current 40mA, step-scan, 1.5 deg/min). Raman (Renishaw InVia Confocal Raman Microscope, 532nm excitation wavelength) spectra was obtained directly from dry particles staged on the microscope. Collected spectra were normalized to ν1 phosphate peak intensity.

A.3.3. Results

Aluminate salt was used as the source of aluminum for these aluminum substituted HAs. With higher concentrations of aluminate, macro-scale size particles different from majority of nanoparticles (other than needle-like and sphere shaped particles) were observed.

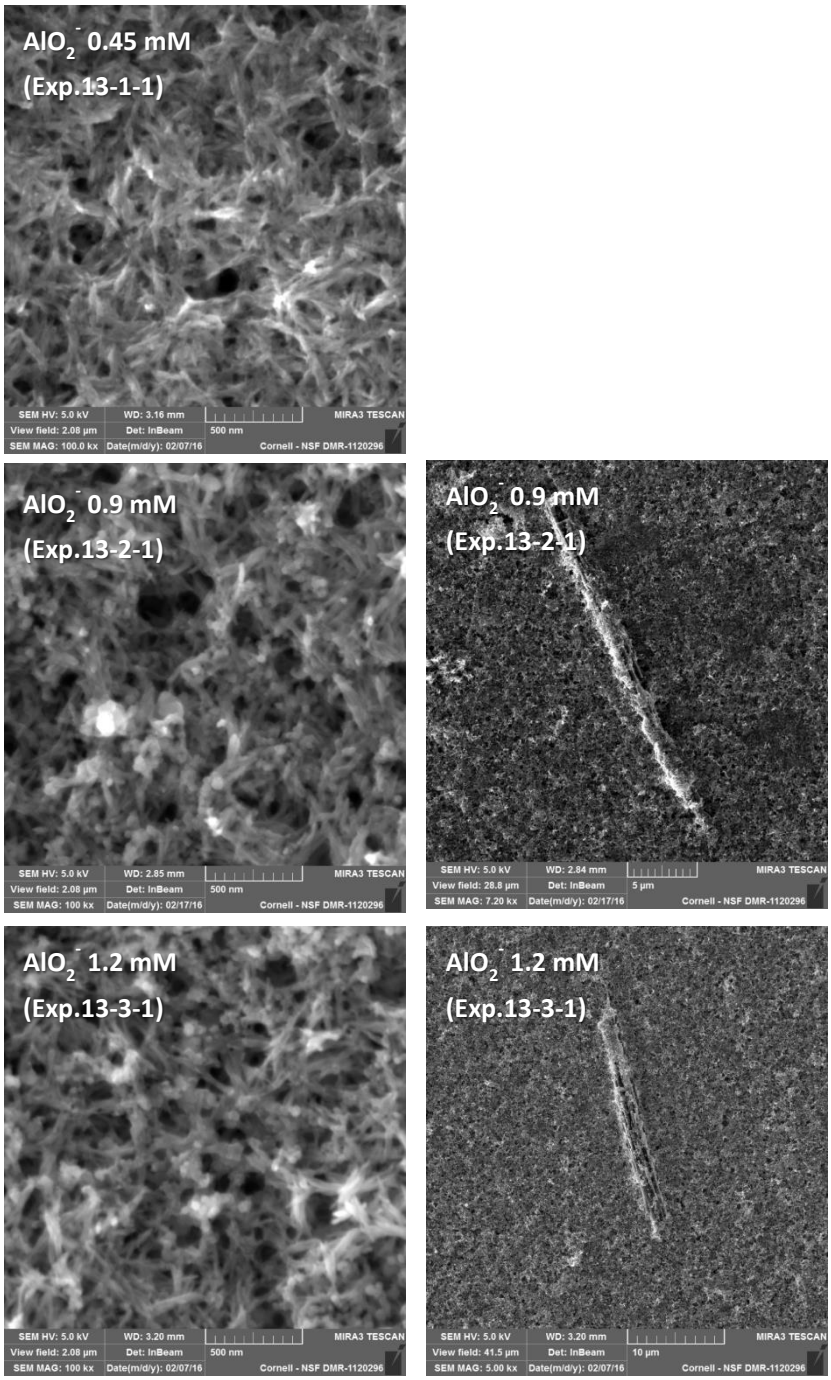

Figure A.3-1. SEM images of particles synthesized with aluminate salt. With high concentrations of aluminate, formation of macro-scale size particles were observed.

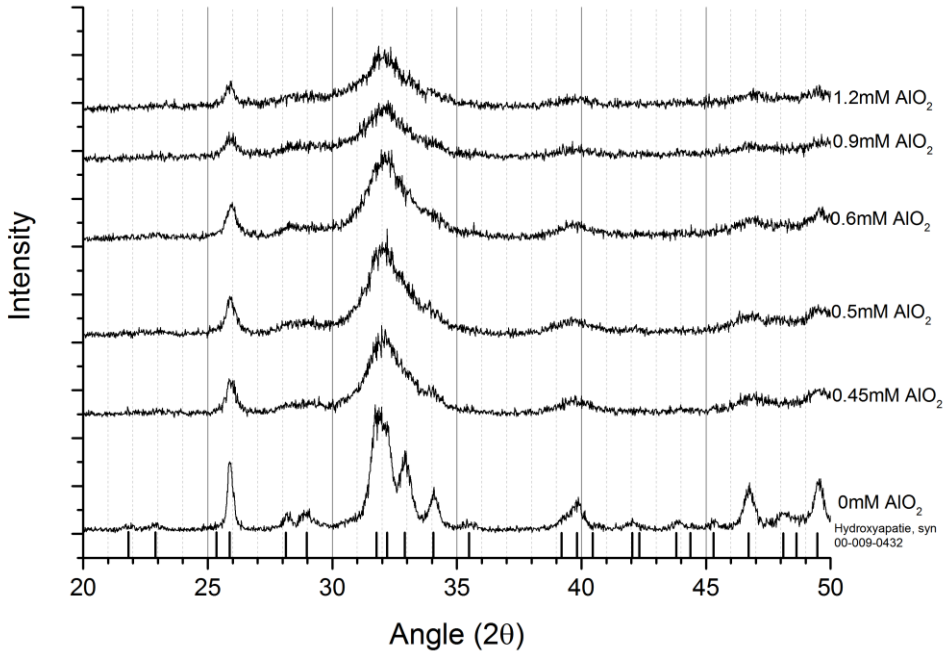

Figure A.3-2. Powder XRD data of particles synthesized with aluminate salt.

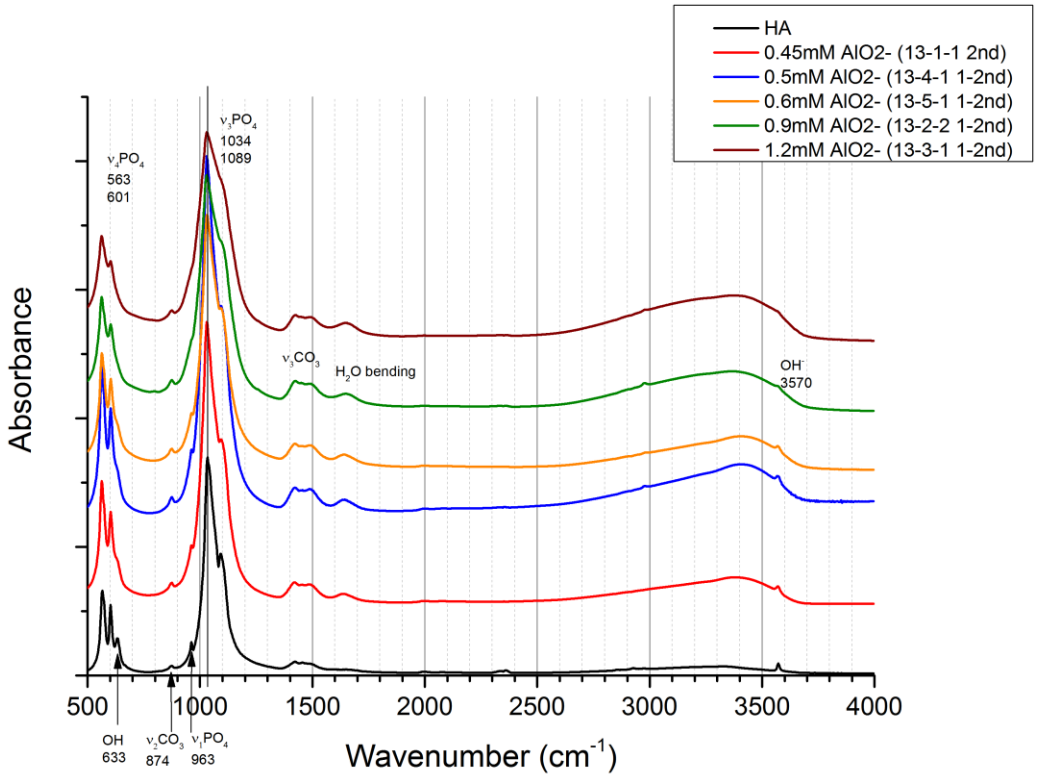

Figure A.3-3. FTIR spectra of particles synthesized with aluminate salt.

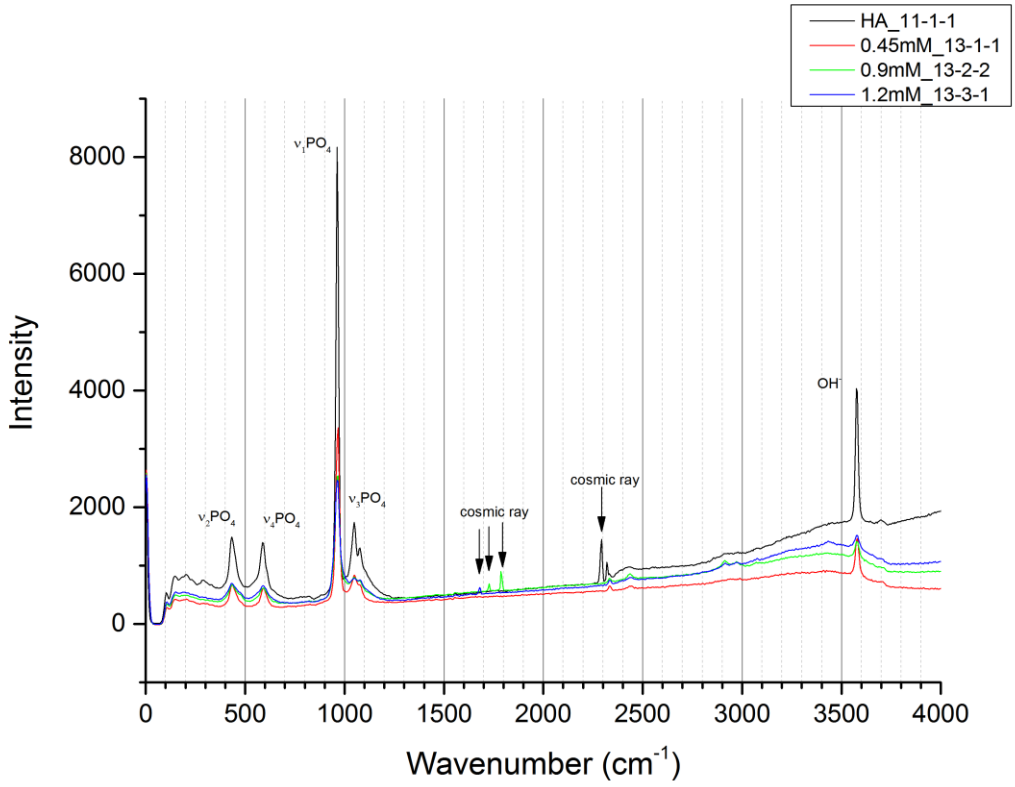

Figure A.3-4. Raman spectra of particles synthesized with aluminate salt.

Appendix 4

Aluminum Substituted Hydroxyapatite Synthesized via Hydrothermal Synthesis

A.4.1. Hydrothermal Particle Synthesis

Particles were synthesized via an aqueous precipitation reaction of calcium salt and phosphate salt [1,2]. Aluminum nitrate ($Al(NO_3)_3 \cdot 9H_2O$) was used as the aluminum source in synthesizing aluminum substituted HA (Al-HA) and aluminum substituted amorphous calcium phosphate (Al-ACP). $Ca(NO_3)_2 \cdot 4H_2O$, $(NH_4)_2HPO_4$, and $Al(NO_3)_3 \cdot 9H_2O$ were all obtained from Sigma-Aldrich, and all reagents were used as received. De-ionized water (18.2 MΩ) was used for all aqueous solutions. For HA synthesis, a 250 mL solution of $(NH_4)_2HPO_4$ was added to a 250 mL solution of $Ca(NO_3)_2 \cdot 4H_2O$ under rapid stirring at room temperature. The final molarity of calcium and phosphate was 5 mM and 3 mM, respectively, with a 500mL reaction volume, to achieve calcium to phosphate ratio of 1.67. After mixing, 80 mL of suspensions were poured into a Teflon vessel and screwed tight in a parrbomb (Parr Instruments, IL, USA). Suspension containing parrbomb was then placed in 180 ^{0}C furnace for 72hrs (Dwell time: 72hrs). Rest of the precipitates were aged in 65 ^{0}C oven for 20 hours. For aluminum substituted HA synthesis, all parameters and procedures were kept the same as the HA synthesis except for addition of $Al(NO_3)_3 \cdot 9H_2O$ in calcium solution to obtain final concentrations of 0.45 mM and 0.9 mM of Al^{3+} ions. After 72 hours of aging for Parrbomb aged particles, crystals were collected via centrifugation (Thermos Scientific Sorvall Legend RT + Centrifuge, 3600 g, 5 min). For oven aged particles, after 20 hours of aging, were collected via

centrifugation (Thermos Scientific Sorvall Legend RT + Centrifuge, 3600 g, 5 min). Collected pellets of particles (parrbomb and oven-aged) were washed with 0.15 M NH_4OH three times. Washed and centrifuged pellets were lyophilized for 72 hours to obtain dry particles.

A.4.2. Particle Characterization

Particles were characterized by scanning electron microscopy (SEM) for shape and morphology. Powder x-ray diffraction (pXRD) was used for obtaining information on material phase and crystallinity. Energy Dispersed X-ray spectroscopy (EDX) was used to map the distributions of elements (Ca, P, and Al) in the particles.
Particles were aliquoted from the final washing step on to a silicon wafer and carbon coated for examination under SEM (Tescan Mira3 FESEM, 5kV). EDX spectroscopy data was obtained right after SEM image acquisitions in the same instrument. The working distance was increased above 15 mm for X-ray detection and beam voltage was raised to 20 kV to maximize counts for efficiency. Dried particles were characterized via pXRD (Scintag Inc. PAD-X theta-theta X-ray Diffractometer, Cu Kα 1.54Å, accelerating voltage 40kV, current 40mA, step-scan, 1.5 deg/min).

A.4.3. Results

Hydrothermal particle syntheses with aluminum resulted in segregation of aluminum species. With high temperature and pressure of reaction, it is shown that aluminum is not incorporated in HA and segregated to crystallize into aluminum oxide

particles. EDX mapping data shows localization of alumimum on macro-scale sized particles and pXRD data shows that these particles are Bohmite (AlO(OH)).

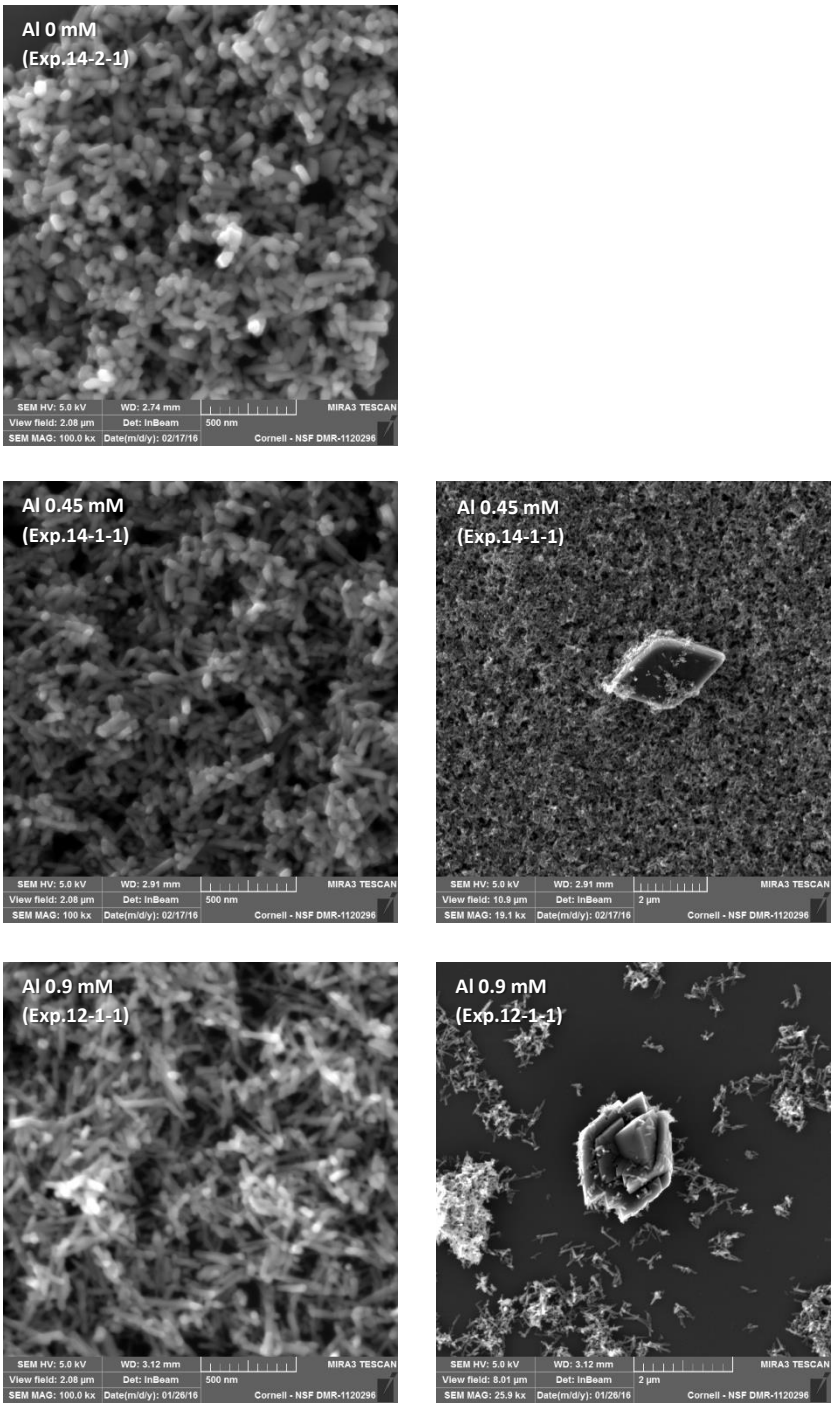

Figure A.4-1. SEM images of particles. Macro-scale particles of Bohmite was observed.

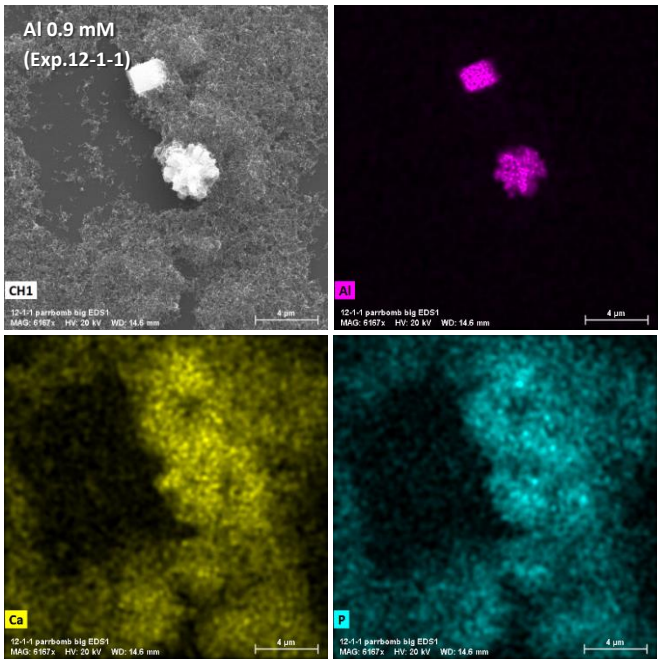

Figure A.4-2. EDX spectroscopy mapping of nanoparticles and macro-scale sized particles. Aluminum is localized on the macro-scale sized particles.

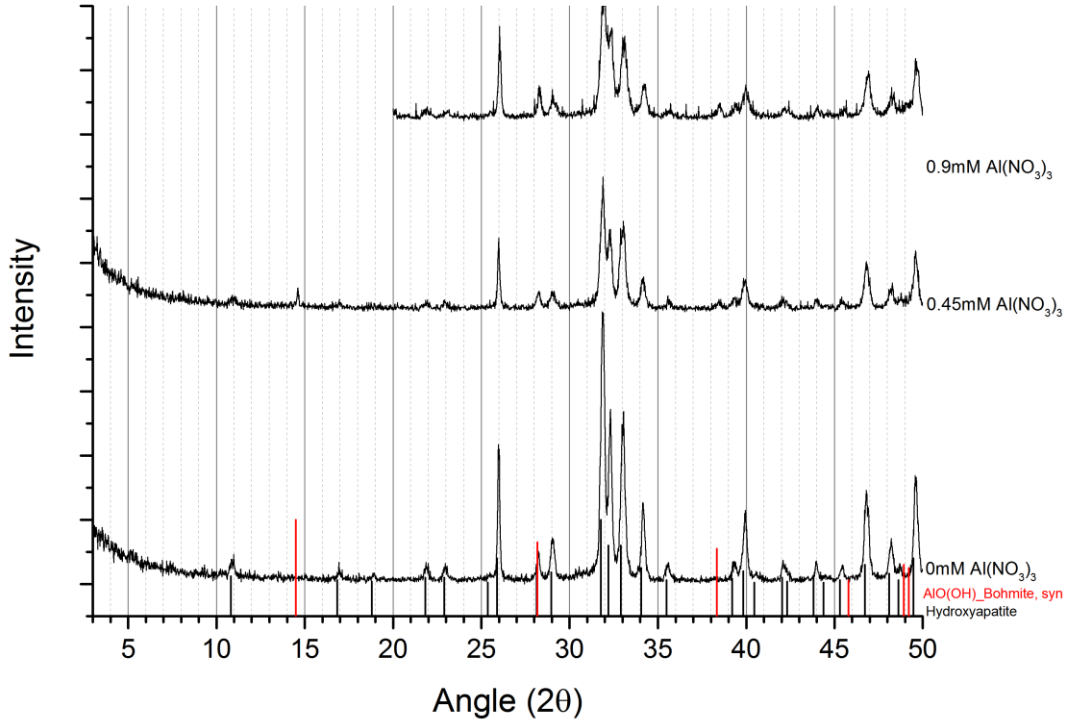

Figure A.4-3. Powder XRD data for hydrothermally synthesized particles. Aluminum concentrations of 0.45 mM and 0.9 mM syntheses shows mixture of HA and Bohmite (AlO(OH)).

Appendix 5

Amorphous calcium phosphate (ACP) synthesis and characterization

A.5.1 Particle Synthesis

Particles were synthesized via an aqueous precipitation reaction of calcium salt and phosphate salt [1–3]. $Ca(NO_3)_2{\cdot}4H_2O$, $(NH_4)_2HPO_4$, and NH_4OH were all obtained from Sigma-Aldrich, and all reagents were used as received. De-ionized water (18.2 MΩ) was used for all aqueous solutions.

For HA synthesis, a 250 mL solution of $(NH_4)_2HPO_4$ was added to a 250 mL solution of $Ca(NO_3)_2{\cdot}4H_2O$ under rapid stirring at room temperature. The final molarity of calcium and phosphate was 5 mM and 3 mM, respectively, with a 500mL reaction volume, to achieve calcium to phosphate ratio of 1.67. Prior to mixing, the pH of all solutions were adjusted to 9.5 using concentrated NH_4OH (28~30wt%). After mixing, the precipitates were aged in 65 ^{0}C oven for 20 hours. After 20 hours of aging, particles were collected via centrifugation (Thermos Scientific Sorvall Legend RT + Centrifuge, 3600 g, 5 min). Collected pellets of particles were washed with 0.15 M NH_4OH three times. Washed and centrifuged pellets were lyophilized for 72 hours to obtain dry particles.

For amorphous calcium phosphate (ACP) synthesis, 9 mL of 0.35 M calcium nitrate solution and 21 mL of 0.158 M ammonium phosphate solutions were prepared and cooled to 4 ^{0}C prior to use. Prepared phosphate solution in a 50 mL beaker was placed in an ice bath under a rapid stir (stir rate ≈ 1150 rpm). Cooled calcium solution

was poured into stirring phosphate solution to obtain precipitations instantaneously. The suspension was centrifuged 3601g at 4 ^{0}C for 3 minutes and washed with 4 ^{0}C DI water (Thermos Scientific Sorvall Legend RT + Centrifuge, 3600g, 5min). The washing procedure was repeated three times and lyophilized for 72 hours to obtain dry particles.

A.5.2. Particle characterization

Particles were aliquoted from the final washing step on to a silicon wafer and carbon coated for examination under SEM (Tescan Mira3 FESEM, 5kV). Dried particles were characterized via pXRD (Scintag Inc. PAD-X theta-theta X-ray Diffractometer, Cu Kα 1.54Å, accelerating voltage 40kV, current 40mA, step-scan, 1.5 deg/min). KBr pellets were prepared for FTIR (Bruker Hyperion FT-IR Spectrometer, 2cm^{-1} resolution, 64 scans) spectra scans. 200mg of FTIR-grade KBr particles (Sigma-Aldrich) and 2mg of synthesized particles were mixed and cold-pressed into pellets. Raman (Renishaw InVia Confocal Raman Microscope, 532nm excitation wavelength) spectra were obtained directly from dry particles staged on a clean glass slide. Collected spectra were normalized to ν1 phosphate peak intensity. KBr pellets were prepared for FTIR (Bruker Hyperion FT-IR Spectrometer, 2cm^{-1} resolution, 64 scans) spectra scans. 200 mg of FTIR-grade KBr particles (Sigma-Aldrich) and 2 mg of synthesized particles were mixed and cold-pressed in to pellets. The spectra were normalized to the ν3 phosphate peak intensity.

A.5.3. Results

Amorphous calcium phosphate particles were synthesized via aqueous precipitation reaction and the reaction temperature was maintained low. Sphere shaped particle morphology and broad band in the pXRD pattern indicates that the particles lack long-range order. From FTIR and Raman spectroscopy, broad bands of phosphate modes further shows lack of local ordering of phosphate groups in the particles.

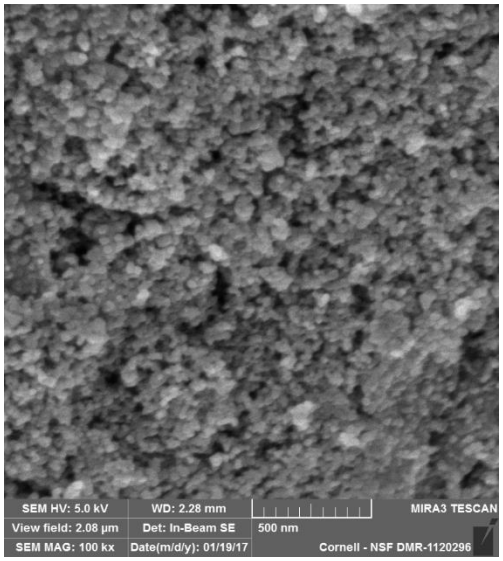

Figure A.5-1. SEM image of ACP particles

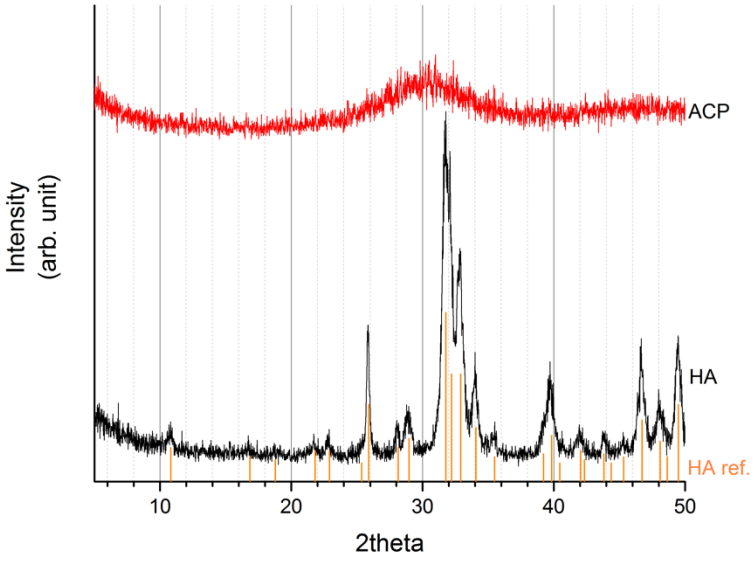

Figure A.5-2. XRD of ACP and HA

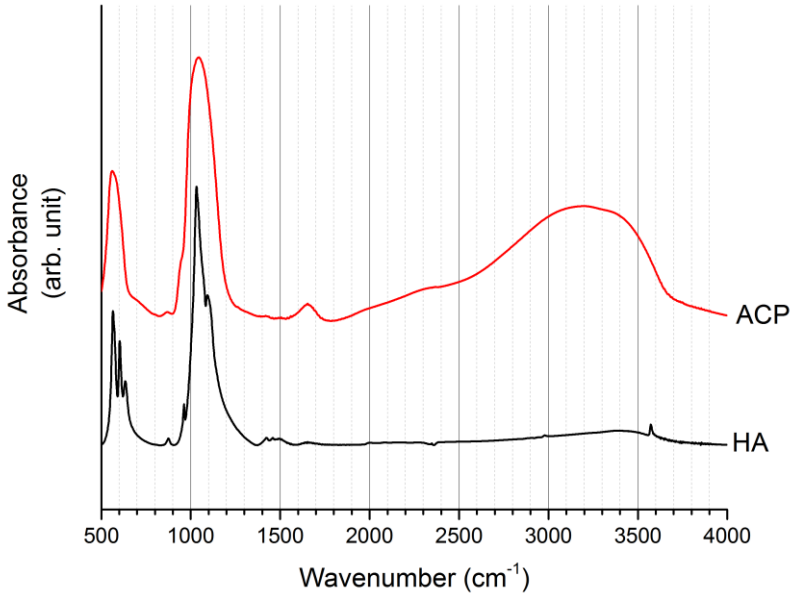

Figure A.5-3. FTIR spectra of ACP and HA

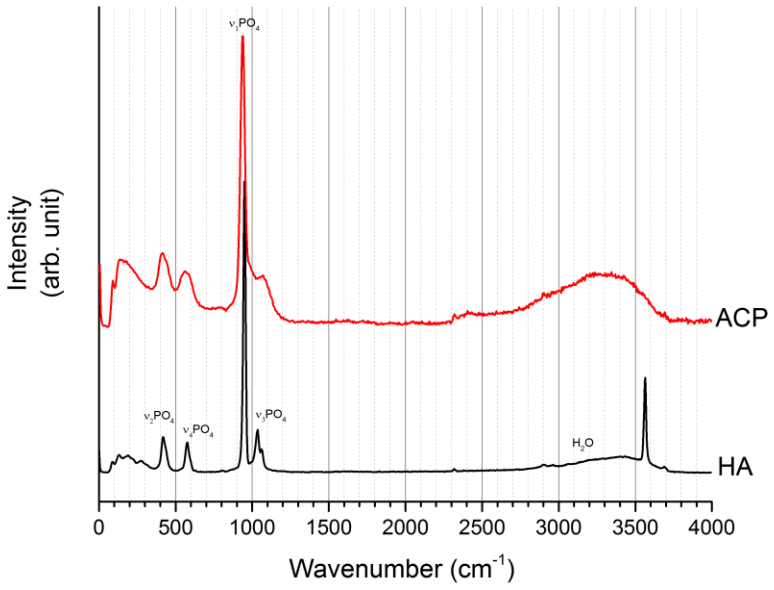

Figure A.5-4. Raman spectra of ACP and HA

Appendix 6

Raman spectroscopy data for aluminum substituted HA

A.6.1 Particle synthesis - Pre-mix pH adjustment / Ammonia (x3) Washing / Lyophilization

Particles were synthesized via an aqueous precipitation reaction of calcium salt and phosphate salt [1,2]. Aluminum nitrate ($Al(NO_3)_3 \cdot 9H_2O$) was used as the aluminum source in synthesizing aluminum substituted HA (Al-HA) and aluminum substituted amorphous calcium phosphate (Al-ACP). $Ca(NO_3)_2 \cdot 4H_2O$, $(NH_4)_2HPO_4$, and $Al(NO_3)_3 \cdot 9H_2O$ were all obtained from Sigma-Aldrich, and all reagents were used as received. De-ionized water (18.2 MΩ) was used for all aqueous solutions. For HA synthesis, a 250 mL solution of $(NH_4)_2HPO_4$ was added to a 250 mL solution of $Ca(NO_3)_2 \cdot 4H_2O$ under rapid stirring at room temperature. The final molarity of calcium and phosphate was 5 mM and 3 mM, respectively, with a 500mL reaction volume, to achieve calcium to phosphate ratio of 1.67. Prior to mixing, the pH of all solutions were adjusted to 9.5 using concentrated NH_4OH (28~30wt%). After mixing, the precipitates were aged in 65^0C oven for 20 hours. For aluminum substituted HA synthesis, all parameters and procedures were kept the same as the HA synthesis except for addition of $Al(NO_3)_3 \cdot 9H_2O$ in calcium solution to obtain a final concentrations ranging from 0.1mM to 1mM of Al^{3+} ions. For Al-HA and Al-ACP, the Al^{3+} concentration is 0.45mM and 0.9mM, respectively. After 20 hours of aging, particles were collected via centrifugation (Thermos Scientific Sorvall Legend RT + Centrifuge, 3600g, 5min). Collected pellets of particles were washed with 0.15 M

NH_4OH three times. Washed and centrifuged pellets were lyophilized for 72 hours to obtain dry particles.

A.6.2. Raman spectroscopy characterization

Raman (Renishaw InVia Confocal Raman Microscope, 532nm excitation wavelength) spectra was obtained directly from dry particles staged on the microscope. Collected spectra were normalized to ν1 phosphate peak intensity.

A.6.3. Results

Increase in aluminum concentration resulted in decrease of local ordering of synthesized materials, which is shown by the broadening of the phosphate peaks. With the increase of aluminum in the particles, there is also increase in the water band at 3000~3500 cm^{-1}, along with decrease in hydroxyl mode at 3565 cm^{-1}.

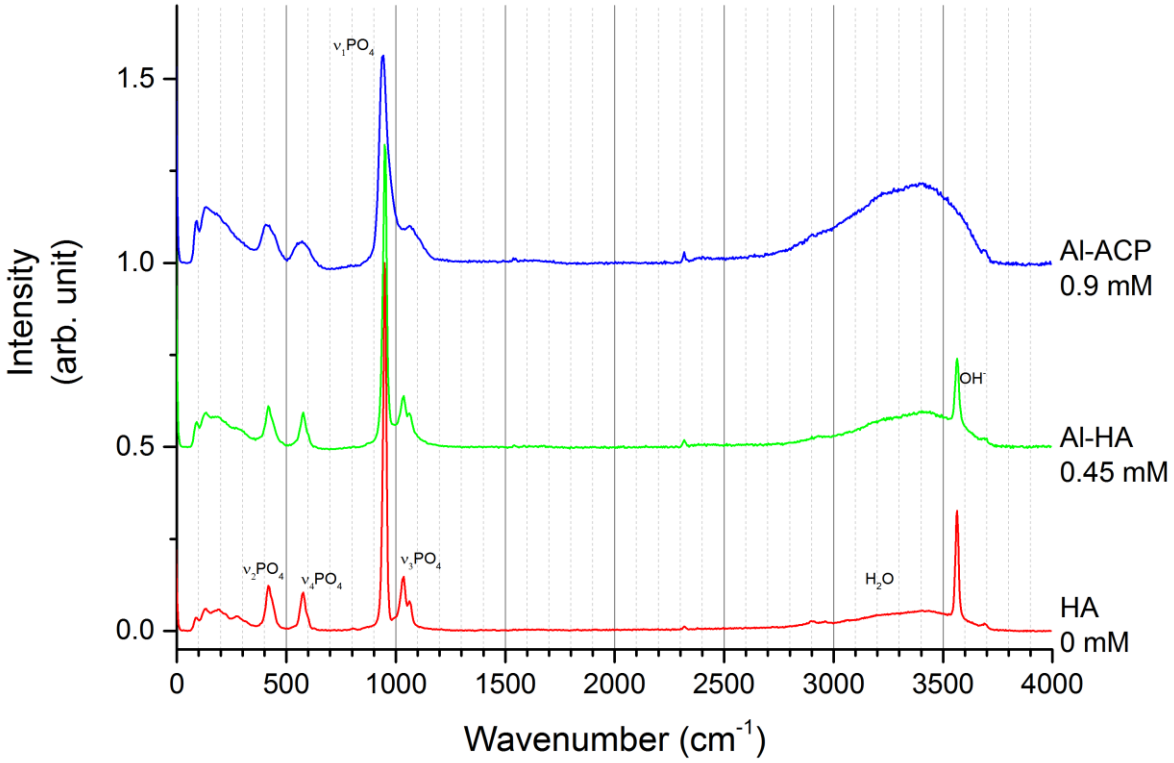

Figure A.6-1. Raman spectra of HA, Al-HA (0.45 mM), and Al-ACP (0.9 mM)

Appendix 7

Co-substitution of Aluminum and Carbonate in Hydroxyapatite

A.7.1. Particle synthesis

Particles were synthesized via an aqueous precipitation reaction of calcium salt and phosphate salt [1,2]. Aluminum nitrate ($Al(NO_3)_3 \cdot 9H_2O$) was used as the aluminum source in synthesizing aluminum substituted HA (Al-HA) and aluminum substituted amorphous calcium phosphate (Al-ACP). $Ca(NO_3)_2 \cdot 4H_2O$, $(NH_4)_2HPO_4$, $Al(NO_3)_3 \cdot 9H_2O$, and $(NH_4)_2CO_3$ were all obtained from Sigma-Aldrich, and all reagents were used as received. De-ionized water (18.2 MΩ) was used for all aqueous solutions.

For HA synthesis, a 250 mL solution of $(NH_4)_2HPO_4$ was added to a 250 mL solution of $Ca(NO_3)_2 \cdot 4H_2O$ under rapid stirring at room temperature. The final molarity of calcium and phosphate was 5 mM and 3 mM, respectively, with a 500mL reaction volume, to achieve calcium to phosphate ratio of 1.67. Prior to mixing, the pH of all solutions were adjusted to 9.5 using concentrated NH_4OH (28~30wt%). After mixing, the precipitates were aged in 65^0C oven for 20 hours.

For carbonate substituted HA synthesis, all parameters and procedures were kept the same as the HA synthesis, except 0.2 mmol ammonium carbonate was added to phosphate solution to obtain final molarity of 0.4 mM at 500 mL reaction volume.

For aluminum substituted HA synthesis, all parameters and procedures were kept the same as the HA synthesis except for addition of $Al(NO_3)_3 \cdot 9H_2O$ in calcium solution to obtain a final concentrations of 0.45 mM of Al^{3+} ions.

For aluminum and carbonate co-substituted HA synthesis, all parameters and procedures were kept the same as the Al-HA synthesis except 0.2 mmol ammonium carbonate was added to phosphate solution to obtain final molarity of 0.4 mM at 500 mL reaction volume.

For all synthesis conditions, after 20 hours of aging, particles were collected via centrifugation (Thermos Scientific Sorvall Legend RT + Centrifuge, 3600g, 5min). Collected pellets of particles were washed with 0.15 M NH_4OH once, and with DI water twice. Washed and centrifuged pellets were lyophilized for 72 hours to obtain dry particles.

A.7.2. Particles Characterization

KBr pellets were prepared for FTIR (Bruker Hyperion FT-IR Spectrometer, $2cm^{-1}$ resolution, 64 scans) spectra scans. 200 mg of FTIR-grade KBr particles (Sigma-Aldrich) and 2 mg of synthesized particles were mixed and cold-pressed in to pellets. The spectra were normalized to the ν3 phosphate peak intensity. Area under ν2 carbonate peak and ν1, ν3 phosphate were calculated to indirectly determine aluminum's substitution quantitatively and qualitatively.

A.7.3. Results

Carbonate is known to substitute phosphate and/or hydroxyl site in HA. This experiment was done to see whether the Al^{3+} ions effect the carbonate substitution and vice versa. Peak area in selected regions of FTIR spectra was done to assess this effect.

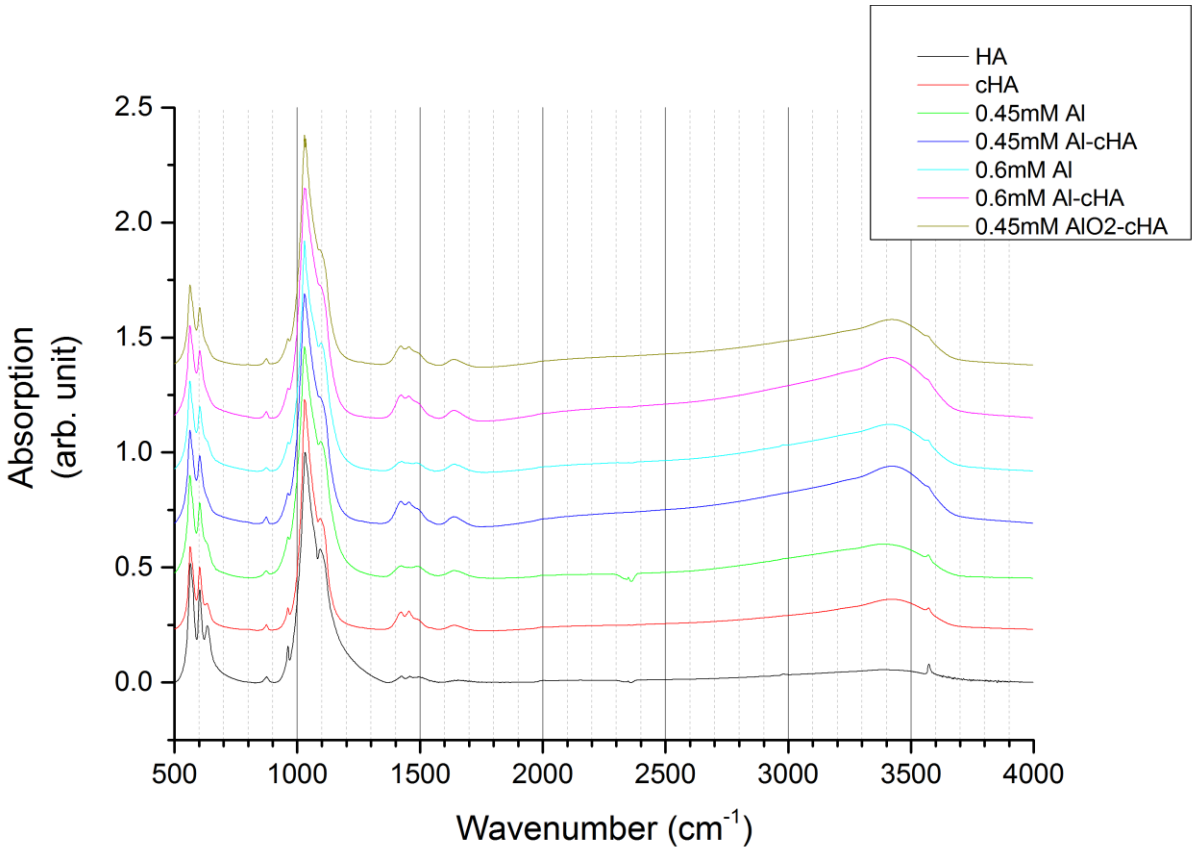

Figure A.7-1. FTIR spectra of aluminum and carbonate co-substituted HA with different concentrations of aluminum and fixed concentrations of carbonate.

Table A.7-2. Area calculation of ν2 carbonate area and ν4 phosphate band region to indirectly determine substitution sites of aluminum.

CO3 area						
Dataset Identifier	Beginning X	Ending X	Max Height	Mathematical Area	Centroid	FWHM
HA	852.50202	889.79095	0.02188	0.38498	873.38661	17.02902
cHA	852.52336	889.17029	0.02356	0.33072	872.81181	12.68344
0.45mM Al	852.50202	889.14804	0.01644	0.28767	871.84401	16.81854
0.45mM Al-cHA	852.52336	889.17029	0.02786	0.43102	872.4415	14.65149
0.6mM Al	852.52336	889.17029	0.01346	0.22959	872.84192	16.39142
0.6mM Al-cHA	852.52336	889.17029	0.02727	0.42662	872.4448	14.85566
0.45mM AlO2-cHA	852.52336	889.17029	0.02375	0.36774	872.51659	14.64122
PO4 area						
Dataset Identifier	Beginning X	Ending X	Max Height	Mathematical Area	Centroid	FWHM
HA	916.79328	1179.10159	0.9241	82.75348	1056.29127	83.86879
cHA	918.10208	1178.48818	0.98134	79.23182	1055.16604	62.37238
0.45mM Al	918.0791	1178.45868	0.93639	93.061	1054.17509	102.85387
0.45mM Al-cHA	918.10208	1178.48818	0.96681	92.99547	1054.01851	95.95737
0.6mM Al	918.10208	1178.48818	0.96009	87.02991	1056.20173	93.68508
0.6mM Al-cHA	918.10208	1178.48818	0.96977	95.68173	1054.79354	101.34986
0.45mM AlO2-cHA	918.10208	1178.48818	0.97036	84.9773	1053.79583	71.35746

Appendix 8

Particle Containing poly(lactic-co-glycolic acid) Scaffold Characterization via X-ray Diffraction

A.8.1. Scaffold Fabrication

3D porous particle containing PLGA scaffolds were fabricated via gas-foaming/particulate leaching methods previously described in the literature[2,4,5]. Briefly, 4mg of PLGA particles (Lakeshore Biomaterials, ground and sieved, average diameter 250 μm), 4mg of PLGA microspheres (synthesized via double emulsion process, diameter 5~50 μm), 8mg of synthesized particles (HA, Al-HA, Al-ACP, ACP), and 152mg of NaCl (JT Baker, sieved to diameter of ~250 μm) were mixed well and cold-pressed under 2 metric tons in a Carver Press (Fred S. Carver Inc.) for 1 minute. Pressed pellets (8mm diameter, 2mm thickness) were pressurized in a pressure vessel (Parr Instruments 4677) under 800psi of carbon dioxide gas for 18 hours, followed by rapid release of pressure resulting in foaming of polymer matrix. Foamed scaffolds were submerged in DI-H_2O for 24 hours to leach out porogenic NaCl particles. Blank PLGA scaffolds were fabricated with the identical parameters and procedures mentioned above with the exception of synthetic particle addition. All scaffolds were sterilized in 70% ethanol for 30 minutes and triple-washed in sterile PBS prior to cell culture.

A.8.2. X-ray Diffraction (XRD) Characterization

Fabricated scaffolds were cold-pressed at 2 metric tons for 5 seconds to obtain flat ~1 mm thickness pellet. The pressed pellet was placed on a XRD sample holder to achieve even level (z-axis) for probing relative to the sample holder to minimize XRD pattern shifts from escalated sample. Minute shifts in the obtained XRD patterns are from differences in probing level.

A.8.3 Scanning Electron Microscopy (SEM) Characterization

Particle morphology and distribution on pore surfaces of the scaffolds were characterized via SEM (LEO 1550, 2kV). Scaffolds were freeze-fractured under liquid nitrogen to expose the pores in the central parts of the scaffolds and mounted on aluminum SEM stubs (Electron Microscopy Sciences) with carbon tape. Samples were subsequently sputter coated using Iridium target. Pore surfaces distant from fractured spots were imaged with SEM to best represent the surfaces interacting with cells.

A.8.4. Results

The diffraction patterns obtained from flattened scaffolds show that the overall particle material quality is maintained (Fig. A.5-1). Amorphous calcium phosphate particles were also used to fabricate scaffolds. Powder XRD data shows that the ACP particles crystallize into HA, and depending on the pH of the salt leaching solvent, the degree of crystallization seems to be effected. SEM imaging of ACP-scaffold pore

surfaces shows that the sphere shape morphology of initial ACP particle was no longer maintained.

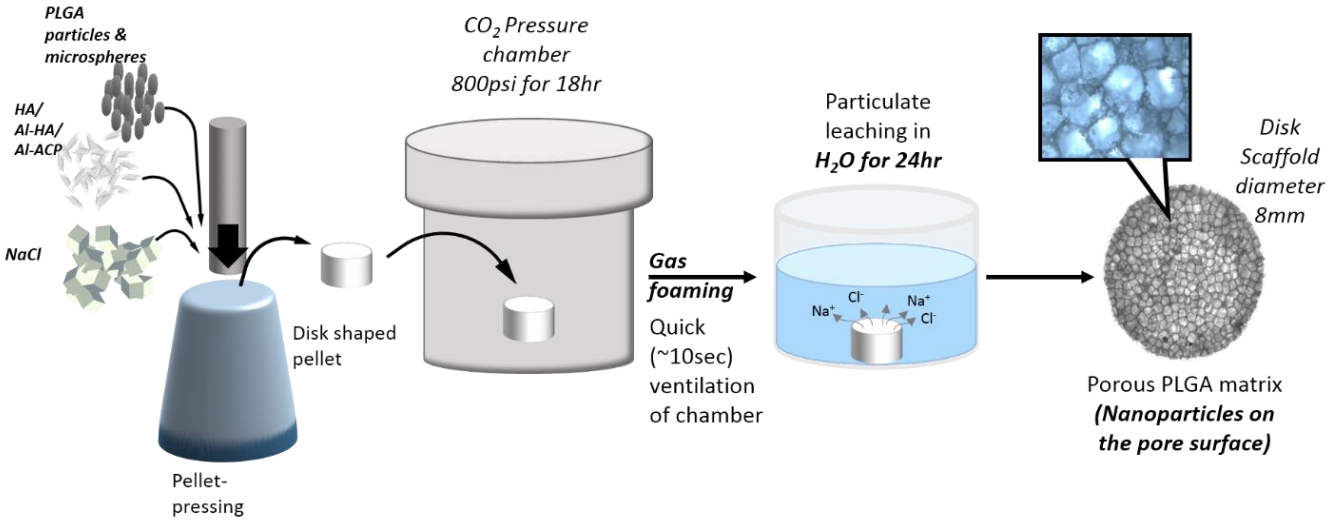

Figure A.8-1. Schematices of scaffold fabrication process.

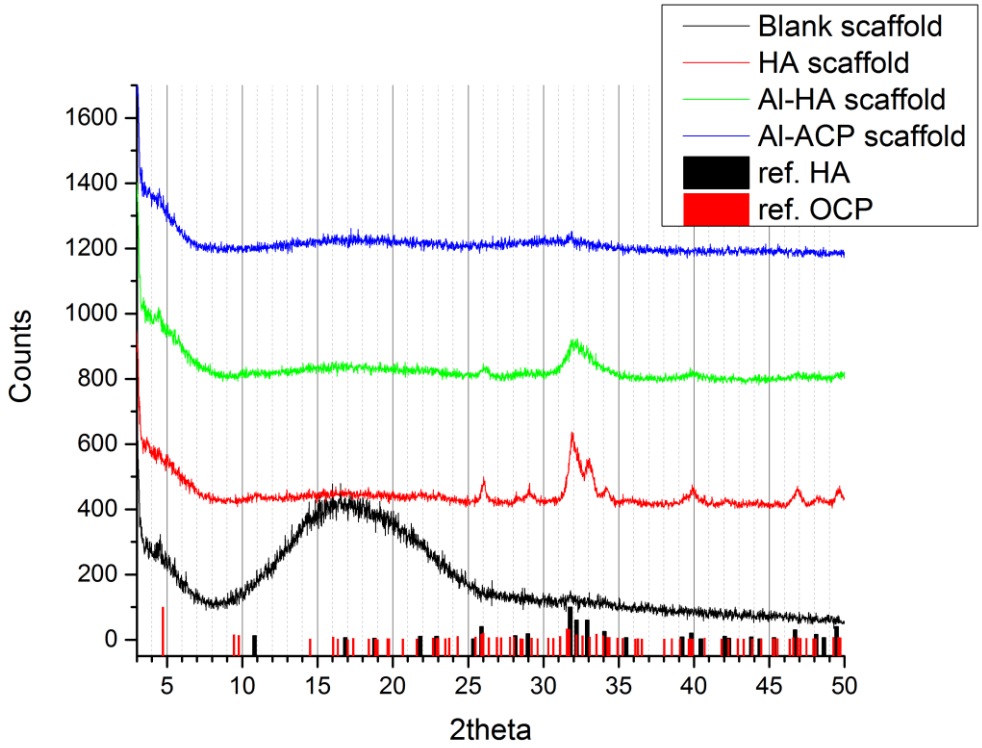

Figure A.8-2. XRD of pressed scaffolds.

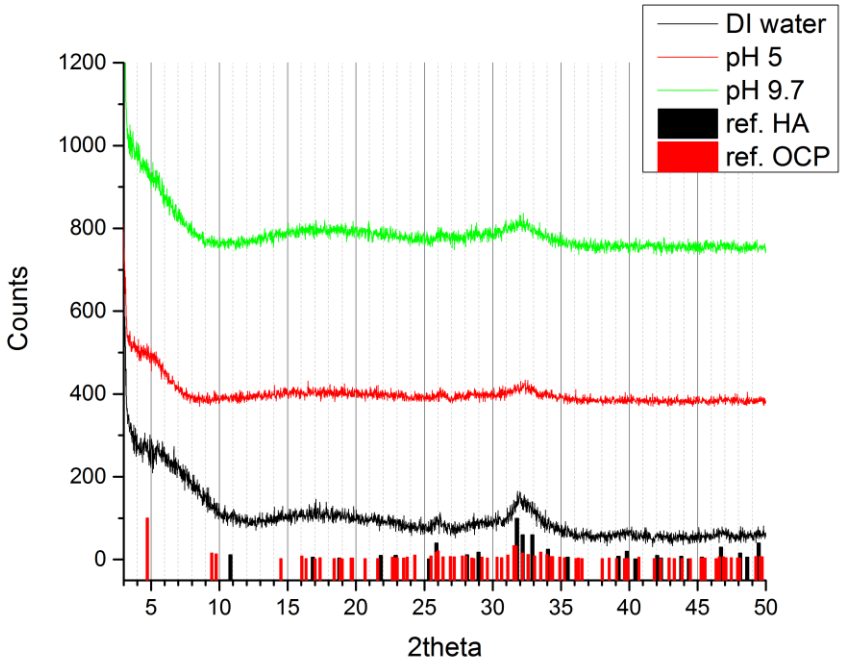

Figure A.8-3. XRD of pressed ACP scaffolds prepared with different pH aqueous solvent for salt leaching.

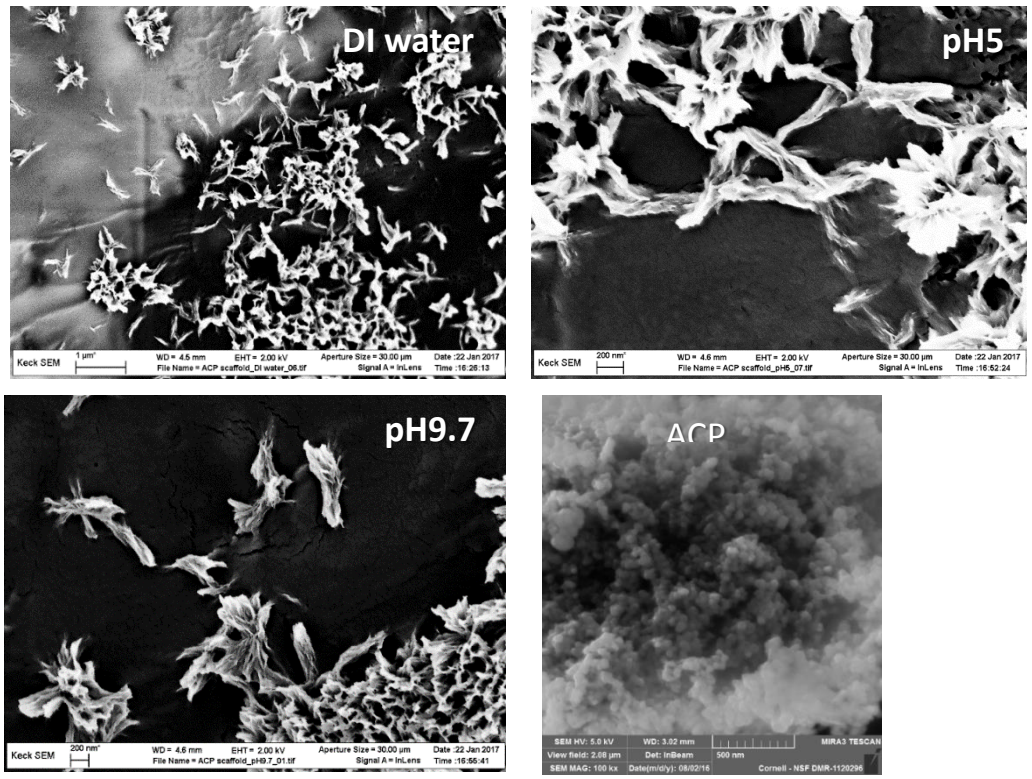

Figure A.8-4. SEM images of ACP scaffold surfaces with different pH salt-leaching solutions. Also, SEM image of ACP particles are shown for reference.

Appendix 9

MDA-MB231 72 hours Cell Culture and IL8 Assay

A.9.1. 72 hours Cell Culture for Growth and IL-8 Quantification

Human MDA-MB231 breast cancer cells (ATCC) were incubated under standard culture conditions (37 ^{0}C, 5% CO_2) in 10% FBS (Tissue Culture Biologicals) supplemented DMEM (Invitrogen) and 1% penicillin/streptomycin (Invitrogen) for 3 days. Sterilized and washed scaffolds were seeded with 1.5 million MDA-MB231 cells and subsequently maintained under dynamic culture condition on an orbital shaker up to 30 min. Cell seeded scaffolds were transferred into 5 mL of DMEM supplemented with 10% FBS in 6-well plates and incubated on an orbital shaker for 48 hrs. The scaffolds were then transferred into fresh 6-well plates with 3mL of 1% FBS supplemented DMEM and incubated for 24 hrs. Cell culture media were collected and centrifuged to obtain supernatants to measure IL-8 secretion. IL-8 from supernatant media was measured via enzyme-linked immunosorbent assay (ELISA; R&D) according to the manufacturer's instructions and normalized to the DNA content. To measure cell growth via DNA quantity, incubated scaffolds were doubly washed in 1mL PBS and lysed in Caron's buffer by sonication. Centrifugation of lysate and scaffold debris were done to collect supernatant DNA content for quantification (QuantiFluor dsDNA System, Promega Corporation).

One-way ANOVA and Student's t-test were used to determine statistical significance among conditions. Tukey's post-hoc test was used for pairwise significance analysis. Significance between the groups and the blank scaffold, HA

scaffold, and Al-HA scaffold are denoted by (*), (#), and (●), respectively. For all pairwise analysis, $p<0.05$ is indicated by single symbol and $p<0.01$ is indicated by double symbols. Cell culture experiments were done in triplicates or more for all conditions. Result data are presented as a mean with error bars representing standard deviations.

A.9.2. Results

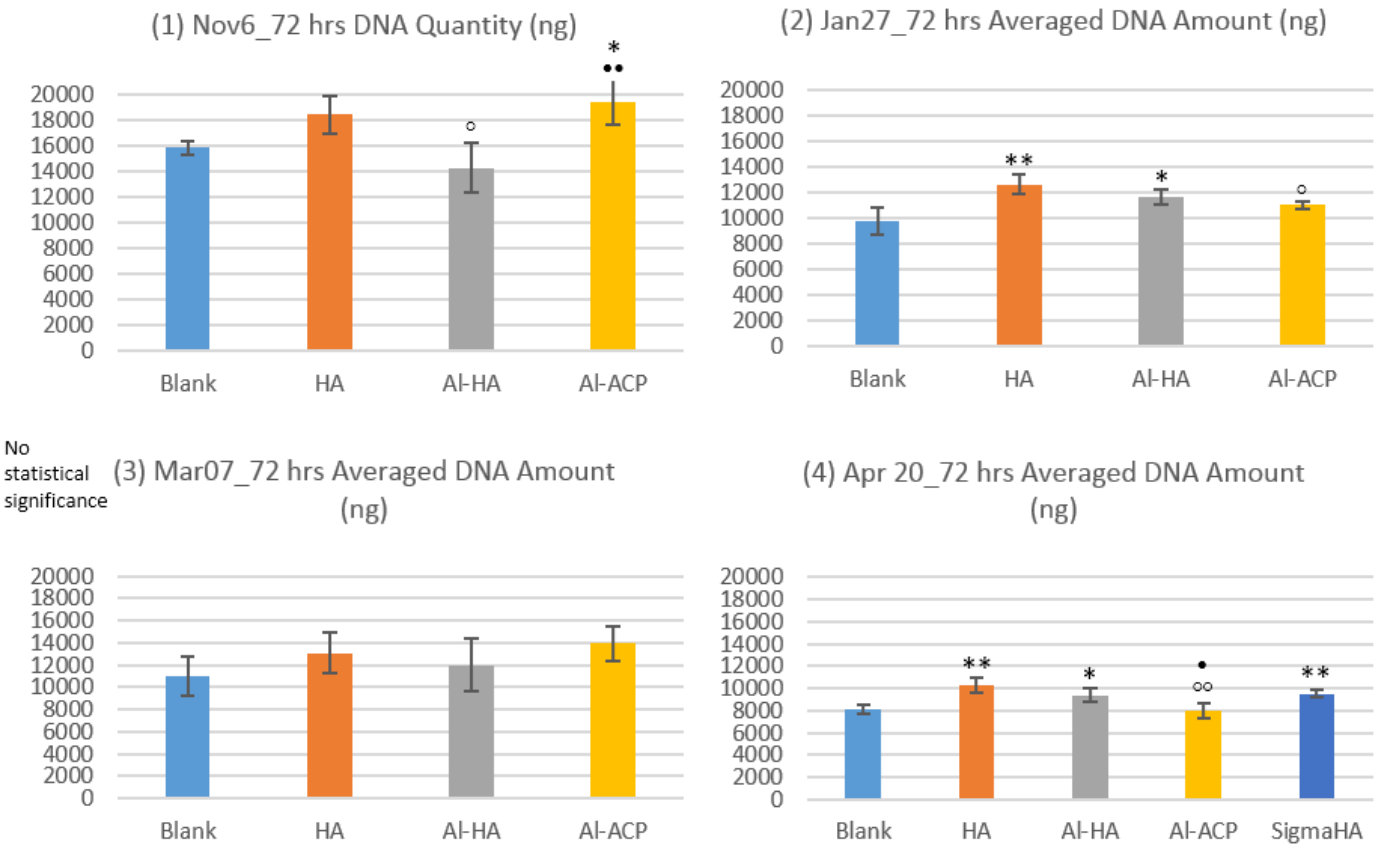

Figure A.9-1. Four DNA quantification to determine cell growth differences depending scaffold condition (Blank, HA, Al-HA, Al-ACP; Sigma HA condition included in Apr 20 assay) Significance between groups and Blank-, HA-, Al-HA-, and Al-ACP-scaffolds are denoted by (*), (○), and (●) respectively. In all cases, $p < 0.05$ is denoted by single symbol and $p < 0.01$ is denoted by double symbols.

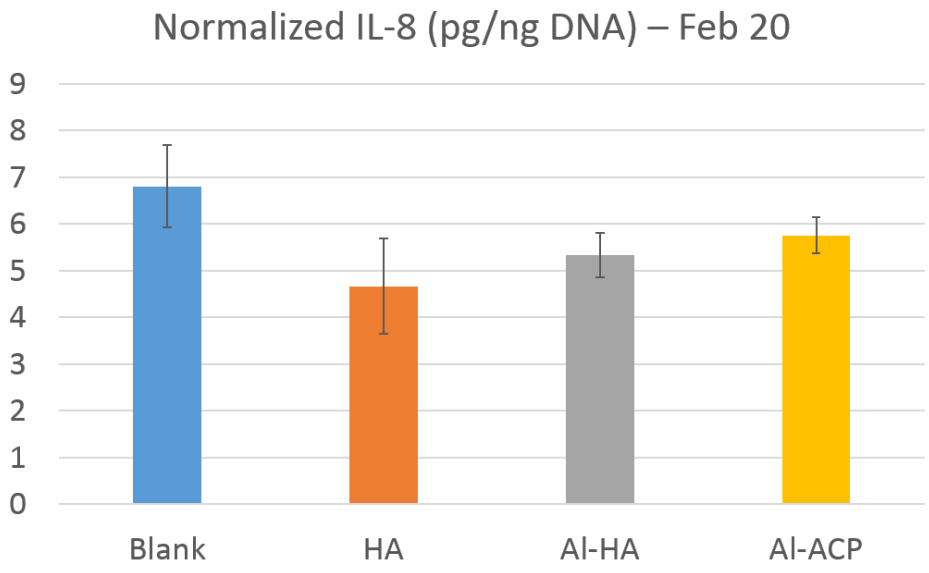

Blank vs	t-test
HA	**0.033565**
Al-HA	**0.033763**
Al-ACP	**0.080718**
HA vs	t-test
Al-HA	0.277145
Al-ACP	**0.092092**
Al-HA s	t-test
Al-ACP	0.215137

Figure A.9-2. IL-8 data normalized by "Jan27" DNA quantification data. Pairwise Student's t-test was done preliminarily assess statistical significance of the data between conditions. P-values under 0.1 is bold-texted.

Appendix 10

MCF-DCIS 72 hours Cell Culture and IL8 Assay

A.10.1. 72 hours Cell Culture for Growth and IL-8 Quantification

Human MCF-DCIS breast cancer cells (ATCC) were incubated under standard culture conditions (37 ^{0}C, 5% CO_2) in 10% FBS (Tissue Culture Biologicals) supplemented DMEM (Invitrogen) and 1% penicillin/streptomycin (Invitrogen) for 3 days. Sterilized and washed scaffolds were seeded with 1.5 million MCF-DCIS cells and subsequently maintained under dynamic culture condition on an orbital shaker up to 30 min. Cell seeded scaffolds were transferred into 5 mL of DMEM supplemented with 10% FBS in 6-well plates and incubated on an orbital shaker for 48 hrs. The scaffolds were then transferred into fresh 6-well plates with 3mL of 1% FBS supplemented DMEM and incubated for 24 hrs. Cell culture media were collected and centrifuged to obtain supernatants to measure IL-8 secretion. IL-8 from supernatant media was measured via enzyme-linked immunosorbent assay (ELISA; R&D) according to the manufacturer's instructions and normalized to the DNA content. To measure cell growth via DNA quantity, incubated scaffolds were doubly washed in 1mL PBS and lysed in Caron's buffer by sonication. Centrifugation of lysate and scaffold debris were done to collect supernatant DNA content for quantification (QuantiFluor dsDNA System, Promega Corporation).

A.10.2. Results

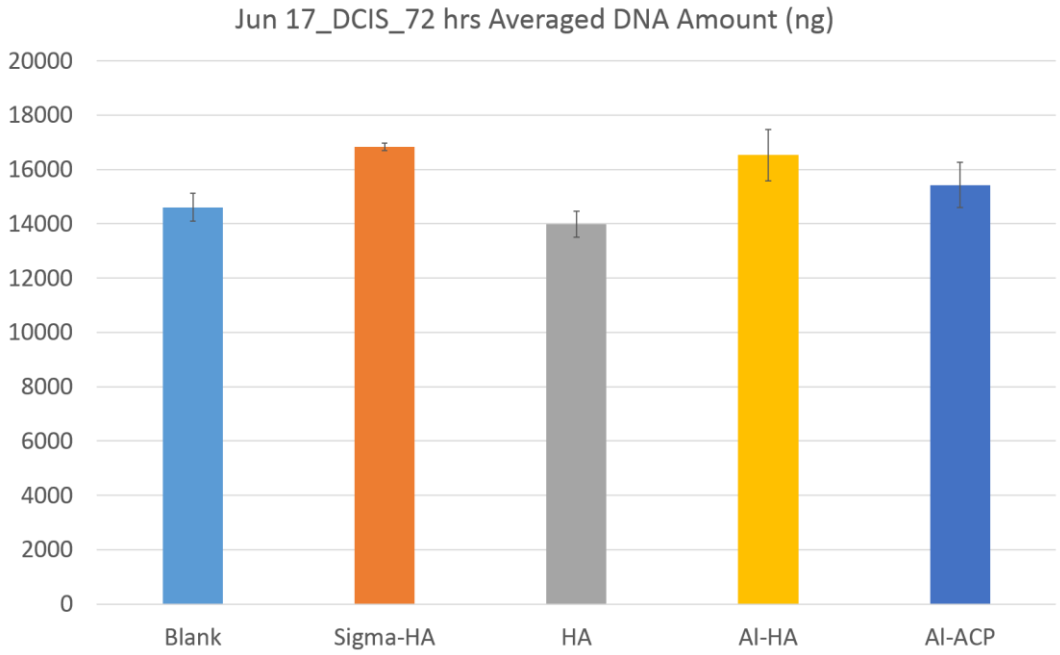

Figure A.10-1. DNA quantification to determine cell growth differences depending scaffold condition (Blank, Sigma HA, HA, Al-HA, Al-ACP). Two scaffolds per condition were seeded to assess DCIS cell response to different conditions of scaffold.

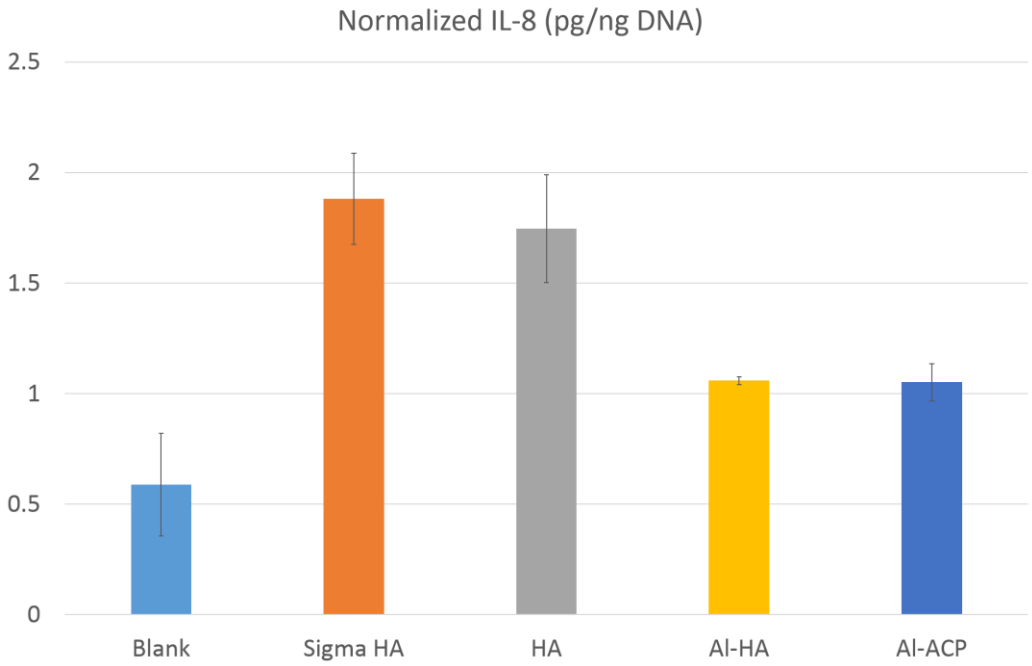

Figure A.10-2. IL-8 data normalized by DNA quantification data. Two scaffolds per condition were seeded to assess DCIS cell response to different conditions of scaffold.

Appendix 11

Alizarin Red Staining of Particle Containing Scaffolds

A.11.1. Alizarin Red Staining

Particle exposure to the surfaces of the scaffold pores were initially assessed with Alizarin Red staining (VWR Life Science). Scaffolds were immersed in 40 mM Alizarin Red staining working solution at room temperature on orbital shaker for 20 minutes. Scaffolds were then removed and washed with DI water twice and dried prior to imaging.

A.11.2. Results

Alizarin Red staining stains for calcium. Staining solution will only interact with the pore surfaces of the scaffolds, which will only stain for calcium containing particles exposed to the pore surfaces. HA, Al-HA, and Al-ACP scaffold all resulted in positive staining of Alizarin Red, indicating that the particles are indeed exposed to the surface and ready to interact with seeded cells. Blank scaffold resulted in negative staining, showing that PLGA polymer does not interact with the stain and shows no significant amount of calcium is in blank scaffolds.

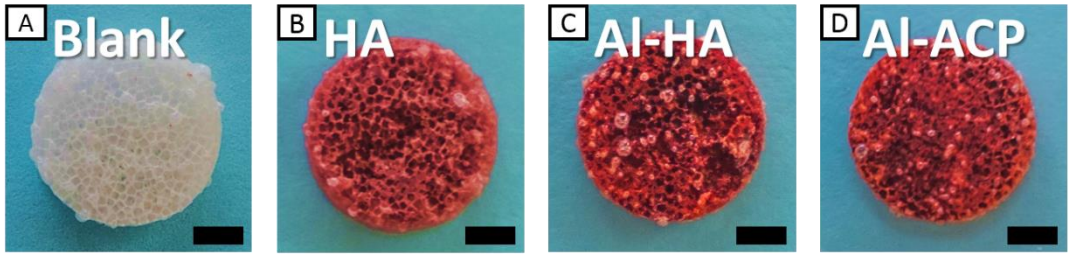

Figure A.11-1. Alizarin Red (AR) staining of scaffolds. Blank scaffold shows negative result to the AR staining. Whereas, HA, Al-HA, and Al-ACP containing scaffolds showed positive results of red staining of the whole scaffolds.

References

1. Wakamura, M., Kandori, K. & Ishikawa, T. Surface structure and composition of calcium hydroxyapatites substituted with Al(III), La(III) and Fe(III) ions. *Colloids Surfaces A Physicochem. Eng. Asp.* **164,** 297–305 (2000).

2. Pathi, S. P., Lin, D. D. W., Dorvee, J. R., Estroff, L. A. & Fischbach, C. Hydroxyapatite nanoparticle-containing scaffolds for the study of breast cancer bone metastasis. *Biomaterials* **32,** 5112–5122 (2011).

3. Somrani, S., Banu, M., Jemal, M. & Rey, C. Physico-chemical and thermochemical studies of the hydrolytic conversion of amorphous tricalcium phosphate into apatite. *J. Solid State Chem.* **178,** 1337–1348 (2005).

4. Lynch, M. E. *et al.* In vivo tibial compression decreases osteolysis and tumor formation in a human metastatic breast cancer model. *J. Bone Miner. Res.* **28,** 2357–2367 (2013).

5. Pathi, S. P., Kowalczewski, C., Tadipatri, R. & Fischbach, C. A novel 3-D mineralized tumor model to study breast cancer bone metastasis. *PLoS One* **5,** 1–10 (2010).